Cell type specificity of mosaic chromosome 1q gain resolved by snRNA-seq in a case of epilepsy with hyaline protoplasmic astrocytopathy

Kun Leng[1], Erron W. Titus[1,2], Nilika Singhal[3], Cathryn R. Cadwell[4,5,6], W. Patrick Devine[4], Tarik Tihan[4], Zhongxia Qi[2], Orit Glenn[7], Sherry Kamiya[4], Amy Berger[8,9], Joseph Shieh[10], Mercedes Paredes[3,6,*], Vaibhav Upadhyay[8,*]

1 - Medical Scientist Training Program, University of California, San Francisco
2 - Department of Laboratory Medicine, University of California, San Francisco
3 - Division of Epilepsy, Department of Neurology, University of California, San Francisco
4 - Department of Pathology, University of California, San Francisco
5 - Department of Neurological Surgery, University of California San Francisco
6 - Weill Institute for Neuroscience, University of California, San Francisco
7 - Department of Radiology and Biomedical Imaging, University of California, San Francisco
8 - Department of Medicine, University of California San, Francisco
9 - Current affiliation: Denali Therapeutics
10 - Medical Genetics, Department of Pediatrics, University of California, San Francisco

*Email: mercedes.paredes@ucsf.edu, vaibhav.upadhyay@ucsf.edu

STRUCTURED ABSTRACT

Introduction:
Mosaic gain of chromosome 1q (chr1q) is a recently described driver of malformation of cortical development (MCD) and epilepsy. Hyaline protoplasmic astrocytopathy (HPA) is a rare neuropathological finding seen in cases of epilepsy with MCD. The cell-type specificity of mosaic chr1q gain in the brain and the molecular signatures of HPA are unknown.

Methods:
We present a child with pharmacoresistant epilepsy who underwent epileptic focus resections at age 3 and 5 years and was found to have mosaic chr1q gain and HPA. We performed single-nucleus RNA-sequencing (snRNA-seq) of brain tissue from the second resection.

Results:
Remarkably, snRNA-seq showed increased expression of chr1q genes only in subsets of neurons and astrocytes. Differentially expressed genes associated with inferred chr1q gain included *AKT3* and genes associated with cell adhesion or migration. A subpopulation of astrocytes demonstrated marked enrichment for synapse-associated transcripts, possibly linked to the astrocytic inclusions observed in HPA.

Discussion:
snRNA-seq may be used to infer the cell type-specificity of mosaic chromosomal copy number changes and identify associated gene expression alterations, which in the case of chr1q gain may involve aberrations in cell migration. Future studies using spatial profiling could yield further insights on the molecular signatures of HPA.

INTRODUCTION

Mosaic chromosome 1 q (chr1q) gain has been recently identified in several case reports and series as a genetic driver of pharmacoresistant epilepsy in the setting of malformation of cortical development (MCD) [1, 2, 3, 4, 5], an umbrella term [6] which encompasses pathologies such as mild MCD (mMCD) with excessive heterotopic neurons [7], focal cortical dysplasia (FCD), gray matter heterotopia, polymicrogyria, and hemimegalencephaly .

Hyaline protoplasmic astrocytopathy is a rare neuropathological finding associated with epilepsy and MCD [8] characterized by protoplasmic astrocytes laden with electron-dense, non-membrane-bound hyaline inclusions reported to have filamin A, GLT-1 (SLC1A2), α-β-crystallin, and cytoglobin immunoreactivity [9, 10].

Here we present a child with pharmacoresistant epilepsy who was found to have mosaic chr1q gain as well as hyaline protoplasmic astrocytopathy from two sequential epileptic focus resection surgeries. We performed single-nucleus RNA-sequencing (snRNA-seq) of brain tissue from the second resection to gain insights into the cell type-specificity of his mosaic chr1q gain and the molecular signatures associated with hyaline protoplasmic astrocytopathy.

METHODS

Research ethics and informed consent

Tissue was acquired and deidentified by the Neurosurgery Tissue Bank at the University of California, San Francisco with patient consent in strict observance of the legal and institutional ethical regulations the UCSF Committee on Human Research (IRB # 10-01318). The tissue was snap frozen in liquid nitrogen in less than 30 minutes after surgical resection.

Single-nucleus RNA-sequencing (snRNA-seq)

snRNA-seq was performed on fresh frozen brain tissue from the patient's second epileptic focus resection. 128 mg of frozen brain tissue was cut at –20 °C and sent on dry ice to Singulomics (New York) for nuclei extraction and snRNA-seq using the 10x Genomics v3 platform, targeting recovery of 10,000 nuclei and 25,000 reads per cell. ~200 million PE150 reads were sequenced on an Illumina NovaSeq 6000 sequencer.

Data analysis

Processing and mapping of raw reads from snRNA-seq and cell calling were performed with Cell Ranger (v7.1.0) using GRCh38-2020-A with inclusion of intronic regions as the reference genome. Analysis of snRNA-seq data was performed in R (v4.3) using Seurat (v5). See Detailed Methods in Supplemental Information.

Data availability

Raw reads and the filtered feature-barcode matrix from snRNA-seq are available on GEO (GSE241521).

RESULTS

Clinical course

Our patient first presented with seizures at 6 months of age. The seizures were characterized by left-sided limb stiffening and gaze deviation, occurring up to one hundred times a day. Scalp EEG revealed right frontal localization, and MRI at 6 months showed non-specific findings without evidence of cortical malformation. The seizures were resistant to standard anti-seizure medications including levetiracetam, oxcarbazepine and clobazam. GeneDx Infantile Epilepsy panel and whole-exome sequencing did not reveal any pathogenic variants. Suppression of seizures was achieved for one year on vigabatrin, with recurrence of seizures on weaning vigabatrin and no response to subsequent medical management. 3T MRI at age 40 months demonstrated very subtle increased T2-FLAIR signal throughout the white matter of the anterior right frontal lobe with minimal blurring of the gray-white border, raising suspicion for FCD (Fig. 1a), which was not visible on 3T MRIs done at age 6 months and 23 months due to incomplete myelination of the frontal lobes. PET scan at age 40 months showed right frontal lobe hypoperfusion (Fig. 1a).

An intraoperative electrocorticography (ECOG)-guided right frontal lobe resection was performed at age 40 months to remove the epileptogenic focus (Fig. 1b). On neuropathology, hyaline protoplasmic astrocytopathy was seen (Fig. 1c,e; Fig. S1). In addition, there appeared to be an abnormal number of heterotopic neurons (> 30/mm^2) in the subcortical white matter without definite cortical dysplasia (Fig. 1d), consistent with the new ILAE classification of mMCD with excessive heterotopic neurons [7]. Genomic analysis of the resected brain tissue using the

UCSF500 Cancer Gene Panel with a buccal swab sample included for comparison revealed an approximate 1.2-fold gain in copy number of chr1q in the resected brain tissue (Fig. 1f) but not in the buccal sample, indicative of mosaic chr1q gain in the brain. The patient continued to have seizures after the initial surgery, and residual right anterior frontal lobe signal abnormalities were seen on repeat MRI. After discussion at multidisciplinary boards and unsuccessful trials of additional medical therapy, the patient underwent a second surgery, a motor-sparing right frontal lobectomy, at age 5 years. The resected tissue from the second surgery demonstrated an approximate 1.05-1.1-fold gain in chr1q copy number, which was lower compared to prior, but with more extensive hyaline protoplasmic astrocytopathy (Fig. 1c). Electron microscopy performed on tissue from the second surgery showed numerous large inclusions composed of electron-dense, non-membrane-bound granular material (Fig 1e). The inclusions appeared to be predominantly in cortical astrocytes and were frequently juxtanuclear, consistent with prior ultrastructural studies of hyaline protoplasmic astrocytopathy [9, 10]. After the second surgery, our patient's seizure frequency improved to approximately once every 10 days on a two-drug anti-seizure medication regimen (clobazam, lamotrigine) continued from prior to the surgery.

Transcriptomic profiling of surgically resected brain tissue

We performed snRNA-seq of fresh frozen brain tissue from our patient's second surgery, recovering nuclear transcriptomes corresponding to 10,764 cells at ~23,000 mean reads per cell and 1,880 median genes detected per cell. After initial clustering and quality control (see Detailed Methods), 10,179 cells were retained for further analysis. Uniform manifold approximation projection (UMAP) of above cells showed well-separated clusters (Fig. 2a) of excitatory (Exc.1-11) and inhibitory (Inh.1-6) neurons, astrocytes (Ast.1-4), oligodendrocytes (Oli.1-2), oligodendrocyte precursor cells (OPC.1-2), microglia (Mic), endothelial cells (End.1-2), and vascular cells (Vas), which all demonstrated expression of appropriate cell type-specific genes (Fig. S2a) and acceptable quality metrics (Fig. S2b).

To infer the cell type-specificity of mosaic chr1q gain, the expression of genes on chr1q was compared to that of all other genes to generate a chr1q module score (see Detailed Methods). We found that chr1q module scores were bimodally distributed, with 10% of cells exceeding the cutoff value of 0.25, which is the chr1q module score corresponding to the local minimum between the two modes in the density plot (Fig. 2b). In contrast, a module score generated with genes from chr1p as a negative control was unimodally distributed (Fig. 2d). Thus, assuming that cells with chr1q module score > 0.25 correspond to cells with chr1q gain and that cells with chr1q gain are trisomic for chr1q, the above estimate of 10% mosaicism would correspond to a bulk fold-change in chr1q copy number of 1.05, consistent with that derived from analysis of the UCSF500 panel data. Plotting the distribution of chr1q module score for each cell type showed bimodality only in excitatory neurons, inhibitory neurons, and astrocytes (Fig. 2e, Fig. S3a**)**, with a Pearson's Chi-squared test *P* value of $< 2.2 \times 10^{-16}$ (Fig. 2f), suggesting that chr1q gain is restricted to neurons and astrocytes.

Differentially expressed genes (DEGs) in cells with inferred chr1q gain compared to those without (see Detailed Methods) showed cell type-specificity (151 upregulated genes specific to excitatory neurons, 23 to inhibitory neurons, and 58 to astrocytes), with 27 upregulated genes shared among all three cell types (Fig. 2g, Fig. S4, Table S1). Among the shared DEGs was *LYST*, a regulator of lysosomal and endosomal trafficking, and *AKT3*, which is located on chr1q (Fig. 1a). Activating somatic mutations in *AKT3* have been associated with epilepsy and MCD and may drive pathology through overactivation of the mTOR pathway [11, 12]. However, we did not recover a significant enrichment for the mTOR pathway in chr1q gain associated DEGs,

which instead demonstrated enrichment for genes involved in cellular adhesion and intercellular junctions (Fig. S5-8, Table S2), processes which are important for cell migration. Given that cortical development requires the appropriate migration of neuronal progenitors, we suspected that chr1q gain associated DEGs in neurons may be involved in cellular migration. Indeed, examination of NCBI and UniProtKB gene summaries of upregulated DEGs shared between excitatory and inhibitory neurons revealed annotations for processes such as cytoskeletal regulation (e.g. *FMN2*), vesicular trafficking, cellular adhesion, and cellular migration (e.g. *ASTN1*); furthermore, there was evidence of regulatory interactions among many of these genes (Fig. 2h).

We next turned our attention to evaluate whether chr1q gain exhibited enrichment in cell type subpopulations by subclustering excitatory neurons, inhibitory neurons, and astrocytes. We found subclusters with marked enrichment of chr1q-gained cells in excitatory neurons (Exc.s6) and astrocytes (Ast.s3, Ast.s4), but not inhibitory neurons (Fig. 2c, Fig. S3b), where chr1q-gained cells were distributed more evenly across subclusters. In excitatory neurons, Exc.s6 compared to all other excitatory neurons demonstrated differential expression of genes involved in neuronal projections (Fig. S9, Table S3-4). In astrocytes, Ast.s3 compared to all other astrocytes demonstrated downregulation of genes involved in glutamate uptake, such as *SLC1A2*, and potassium transport, such as *KCNIP4* (Fig. S10, Table S2). Notably, Ast.s4 compared to all other astrocytes demonstrated a striking enrichment of synapse-associated transcripts such as *SHISA9*, *GRIA1*, *GRIN2A*, *GRIN2B*, *NGLN1*, and *NRXN3* [13] in conjunction with upregulation of *HSP90AA1* (Fig. 3a-c, Fig. S11, Table S3-4), which encodes the Hsp90 chaperone.

DISCUSSION

With respect to the clinical findings, the somewhat lower magnitude of chr1q copy number gain as measured by the UCSF 500 NGS panel in tissue from the second surgical resection compared to the first may reflect a correspondence between the degree of chr1q gain mosaicism and anatomical proximity to the epileptic focus. A similar hypothesis has been validated in the setting of FCD and the rate of mosaic somatic mutations in mTOR pathway genes [14].

With respect to our results from snRNA-seq, our analysis demonstrates that snRNA-seq of archived fresh frozen brain tissue could be used to infer the cell type-specificity of mosaic chromosomal copy number variations and their associated alterations in gene expression. Thus, in this context, single-cell transcriptomics provides a powerful complementary approach to traditional methods such as karyotyping (limited to cells proliferating culture) or FISH. For our patient, tissue culture of freshly isolated primary cells from the second surgery was severely limited by yield, and FISH performed on cultured cells failed to identify any cells with chr1q copy number gain. Per expert consultation, we did not attempt FISH on FFPE samples due to expected technical challenges (such as cutting artifacts, cell overlap, and unclear cell morphology) that limit sensitivity in the setting of low-level mosaic copy number changes.

The enrichment of chr1q gain associated DEGs for genes involved in cell adhesion and migration suggests that chr1q gain disrupts the developmental migration of neuronal and glial

progenitor cells, which is supported clinically by white matter T2-FLAIR hyperintensity with blurring of the gray-white border in the right frontal horn on MRI and the appearance of increased heterotopic neurons in subcortical white matter on neuropathology. Although excitatory neurons and inhibitory neurons are traditionally thought to arise from distinct pools of precursor cells originating from different regions of the developing brain [15], the presence of chr1q gain in both excitatory and inhibitory neurons (as well as astrocytes) in our patient is in line with the recent finding that a subset of cortical progenitor cells can potentially give rise to both excitatory and inhibitory neurons during human brain development [16]. The hypothesis that chr1q gain occurred in a cortical progenitor cell during neurodevelopment would also be consistent with *in vitro* data showing that chr1q gain confers a proliferative advantage in neural stem cells [17]. Lastly, the existence of a subpopulation markedly enriched in chr1q-gained cells in excitatory neurons (Exc.s6) but not inhibitory neurons suggests that migration defects may be more pronounced in excitatory neurons compared to inhibitory neurons.

With respect to astrocytes, chr1q gain may disrupt homeostatic astrocyte functions such as glutamate uptake and potassium buffering (as seen in Ast.s3), which may contribute to epilepsy. Furthermore, our discovery of a subpopulation of astrocytes with inferred chr1q gain demonstrating marked enrichment of synapse-associated transcripts (Ast.s4) suggests that these astrocytes may have been involved in synaptic regulation, such as by pruning or phagocytosis of synaptic debris [18]. We speculate that with cytoskeletal, vesicular trafficking, and lysosomal abnormalities secondary to chr1q gain, these astrocytes may have exceeded their degradative or intracellular trafficking capacity, which may contribute to the inclusions observed in protoplasmic astrocytes on neuropathology and electron microscopy.

In summary, we identified cell type-specific changes in gene expression associated with chr1q gain and possibly hyaline protoplasmic astrocytopathy in our patient, which pointed towards cellular pathways potentially affected by these pathologies. Ultimately, spatial transcriptomics and proteomics will further elucidate the molecular signatures and dysregulated cellular functions associated with hyaline protoplasmic astrocytopathy.

ACKNOWLEDGMENTS

We thank Dr. Alyssa Reddy, Dr. Danilo Bernardo, and Dr. Kurtis Auguste for their involvement in the clinical care of our patient. We thank Dr. Biswa Ramani for assistance with neuropathology interpretation. We thank Julia S. Chu for assisting with storage of clinical samples. We thank Dr. Clifford Lowell, chair of Laboratory Medicine at UCSF, for funding support. KL was supported by NIA F30AG066418. EWT was supported by Damon Runyon Fellowship DRG122-22. VU was supported by NHLBI K08HL165106. CRC was supported by NINDS K08NS126573 and U01NS132353, the Weill Neurohub, the Shurl and Kay Curci Foundation, and Citizens United for Research in Epilepsy (CURE).

CONFLICTS OF INTEREST STATEMENT

AB is currently employed at Denali Therapeutics but was not affiliated with Denali during her clinical involvement with the patient. The authors have no other conflicts of interests to disclose.

262 **REFERENCES**
263

264 1. Kobow, K. *et al.* Mosaic trisomy of chromosome 1q in human brain tissue associates with
265 unilateral polymicrogyria, very early-onset focal epilepsy, and severe developmental delay. *Acta*
266 *Neuropathol.* **140**, 881–891 (2020).

267 2. Conti, V. *et al.* Focal dysplasia of the cerebral cortex and infantile spasms associated with
268 somatic 1q21.1-q44 duplication including the AKT3 gene. *Clin. Genet.* **88**, 241–247 (2015).

269 3. Bedrosian, T. A. *et al.* Detection of brain somatic variation in epilepsy-associated
270 developmental lesions. *Epilepsia* **63**, 1981–1997 (2022).

271 4. Poduri, A. *et al.* Somatic activation of AKT3 causes hemispheric developmental brain
272 malformations. *Neuron* **74**, 41–48 (2012).

273 5. López-Rivera, J. A. *et al.* The genomic landscape across 474 surgically accessible
274 epileptogenic human brain lesions. *Brain* **146**, 1342–1356 (2023).

275 6. Severino, M. *et al.* Definitions and classification of malformations of cortical
276 development: practical guidelines. *Brain* **143**, 2874–2894 (2020).

277 7. Najm, I. *et al.* The ILAE consensus classification of focal cortical dysplasia: An update
278 proposed by an ad hoc task force of the ILAE diagnostic methods commission. *Epilepsia* **63**,
279 1899–1919 (2022).

280 8. Prayson, R. A. Hyaline protoplasmic astrocytopathy: A clinicopathologic study. *Am. J.*
281 *Clin. Pathol.* **146**, 503–509 (2016).

282 9. Hazrati, L.-N. *et al.* Astrocytic inclusions in epilepsy: expanding the spectrum of
283 filaminopathies. *J. Neuropathol. Exp. Neurol.* **67**, 669–676 (2008).

284 10. Hedley-Whyte, E. T. *et al.* Hyaline protoplasmic astrocytopathy of neocortex. *J.*
285 *Neuropathol. Exp. Neurol.* **68**, 136–147 (2009).

286 11. Baldassari, S. *et al.* Dissecting the genetic basis of focal cortical dysplasia: a large cohort
287 study. *Acta Neuropathol.* **138**, 885–900 (2019).

288 12. Pirozzi, F. *et al.* Profiling PI3K-AKT-MTOR variants in focal brain malformations reveals
289 new insights for diagnostic care. *Brain* **145**, 925–938 (2022).

290 13. Glock, C. *et al.* The translatome of neuronal cell bodies, dendrites, and axons. *Proc Natl*
291 *Acad Sci USA* **118**, (2021).

292 14. Checri, R. *et al.* Detection of brain somatic mutations in focal cortical dysplasia during
293 epilepsy presurgical workup. *Brain Commun.* **5**, fcad174 (2023).

294 15. Stoufflet, J., Tielens, S. & Nguyen, L. Shaping the cerebral cortex by cellular crosstalk. *Cell*
295 **186**, 2733–2747 (2023).

296 16. Delgado, R. N. *et al.* Individual human cortical progenitors can produce excitatory and
297 inhibitory neurons. *Nature* **601**, 397–403 (2022).

298 17. Mehrjardi, N. Z. *et al.* Acquisition of chromosome 1q duplication in parental and
299 genome-edited human-induced pluripotent stem cell-derived neural stem cells results in their
300 higher proliferation rate in vitro and in vivo. *Cell Prolif.* e12892 (2020) doi:10.1111/cpr.12892.

301 18. Chung, W.-S. *et al.* Astrocytes mediate synapse elimination through MEGF10 and MERTK
302 pathways. *Nature* **504**, 394–400 (2013).

FIGURE LEGENDS

Fig. 1 | Right frontal lobe abnormalities on neuroimaging, hyaline protoplasmic astrocytopathy on neuropathology, and evidence of mosaic chr1q gain on analysis of the UCSF 500 Cancer Gene Panel. a, 3T T2-FLAIR MR image (left) at age 40 months demonstrating subtle increased hyperintensity in the right frontal white matter with minimal blurring of the gray-white border suggestive of FCD; PET image (right) at age 3 years demonstrating hypoperfusion in the right frontal lobe. **b**, Intra-operative electrocorticography recording from the surgery at age 3 years demonstrating right frontal localization of epileptiform activity; the electrode array (4x5 grid, 20 electrodes) was placed over the right frontal lobe (see Detailed Methods in Supplemental Information). **c**, H&E sections of surgically resected cortical tissue from the surgeries at age 3 and 5 years demonstrating worsened hyaline protoplasmic astrocytopathy over time. Scale bar, 100 μm. **d**, MAP2 immunohistochemistry of white matter in resected cortical tissue at age 3 years demonstrating numerous heterotopic neurons. Scale bar, 100 μm. **e**, Electron microscopy of resected cortical tissue at age 5 years demonstrating an electron-dense cytoplasmic inclusion in an astrocyte. Scale bar, 2 μm. **f**, Visualization of relative read density (top) and minor allele frequency of common single nucleotide polymorphisms (bottom) from the UCSF 500 Cancer Gene Panel performed on surgically resected brain tissue from the surgery at age 3 years. Regions highlighted in blue in the top subpanel reflect regions of chr1q with definitive copy number gain whereas regions highlighted in red reflect regions with possible copy number loss; the jagged appearing black line in the top subpanel corresponds to the running average of the relative read density, and the horizontal black lines in the top subpanel correspond to the average relative read density within corresponding genomic regions.

Fig. 2 | Mosaic chr1q gain in neurons and astrocytes and associated alterations in gene expression identified by snRNA-seq. a, Uniform manifold approximation projection (UMAP) of cells recovered from snRNA-seq, colored by cell cluster assignment (left) or chr1q module score (right). **b**, Density plot of the distribution of chr1q module scores across all cells, plotted on a linear (top) or logarithm (bottom) scale, with the cutoff value of 0.25 highlighted as a dashed vertical line. **c**, UMAP of excitatory neuron, inhibitory neuron, and astrocyte subclusters colored by subcluster assignment or chr1q module score. **d**, Density plot of the distribution of chr1p module score across all cells, plotted on a linear (top) or logarithmic (bottom) scale. **e**, Density plots of the distribution of chr1q module scores in each cell type, in logarithmic scale. **f**, Contingency table of number of cells with (chr1q module score > 0.25) vs without (chr1q module score < 0.25) inferred chr1q gain in each cell type, with the *P* value from Pearson's Chi-squared test shown below. **g**, Venn diagrams of upregulated (left) or downregulated (right) differentially expressed genes (DEGs) associated with chr1q gain in excitatory neurons, inhibitory neurons, and astrocytes. **h**, Network visualization of chr1q gain associated upregulated DEGs shared between excitatory and inhibitory neurons grouped by function. Lines connecting genes reflect evidence of regulatory relationships (see detailed methods in Supplemental Information). Exc – excitatory neurons, Inh – inhibitory neurons, Ast – astrocytes, Oli – oligodendrocytes, OPC – oligodendrocyte precursor cells, Mic – microglia, End – endothelial cells, Vas – vascular cells.

Fig. 3 | A subpopulation of astrocytes enriched in synapse-associated transcripts identified on subclustering. a, UMAP of astrocyte subclusters colored by log-scaled expression score of selected synapse-associated transcripts. **b**, Enriched terms from the ChEA, ARCHS4, Reactome, and GO Cellular Component gene set libraries (see Detailed Methods in Supplemental Information) for genes upregulated in Ast.s4 compared to other astrocytes. **c**, Network visualization of upregulated genes in Ast.s4 that have known regulatory relationships with Hsp90 (*HSP90AA1*) or with those that have a known regulatory relationship with Hsp90.

Supplemental Information for

Cell type-specificity of mosaic chromosome 1q gain resolved by single-nucleus RNA-seq in a case of pharmacoresistant epilepsy associated with hyaline protoplasmic astrocytopathy

DETAILED METHODS

Intraoperative electrocorticography

Following a right frontotemporoparietal craniotomy under local anesthesia using nitrous oxide, narcotics, and dexmedetomidine, the cortical surface was exposed. The brain appeared grossly intact. A 5x4 array of 20 electrodes numbered 1 through 20 was placed over the right frontal lobe with the following orientation: 20 - anterior inferior, 1 - posterior superior, 5 - anterior superior, 16 - posterior inferior, motor strip - 1, 6, 11. Recording from these electrodes revealed a background consisting of low-amplitude theta frequency activity with superimposed faster elements.

Electron microscopy

Freshly harvested tissue was minced into pieces < 2 mm in width. Tissue pieces were fixed with glutaraldehyde in cacodylate buffer and then stored in cacodylate buffer. Osmium tetraoxide was used for secondary fixation, followed by dehydration and resin embedding. Thin sections were stained with uranyl acetate and lead citrate. Images were collected by the UCSF Pathology department electron microscopy service.

UCSF 500 Cancer Gene Panel

The UCSF 500 Cancer Gene Panel is an exon-capture-based panel that targets 529 genes plus additional genome-wide probes to detect gross chromosomal gains or losses. The test is available to patients through the UCSF Clinical Cancer Genomics Lab (CPT code 81455). For visualization of chromosomal-level copy-number variations, the $\log_2$ value of the ratio of sample coverage over pooled normal coverage is plotted in Fig. 1c. The pooled normal coverage is derived from ~300 samples that were processed and sequenced in the same pipeline as the sample.

snRNA-seq data analysis

The filtered feature-barcode matrix of raw UMI counts generated by CellRanger after alignment of raw reads was loaded into Seurat (v4.9.9). Data normalization and identification of highly variable genes was performed using Seurat::SCTransform with default parameters. The resulting Pearson residuals from SCTransform's negative binomial generalized linear model correcting for variation in library size among cells (the 'scale.data' slot in the 'SCT' assay) corresponds to the "log-scaled expression score" used for differential expression analysis and gene expression visualization referenced in the manuscript and described below. Dimensionality reduction and initial clustering was performed using Seurat::RunPCA, Seurat::RunUMAP, Seurat::FindNeighbors, and Seurat::FindClusters with default parameters, specifying a range of values for the resolution parameter for Seurat::FindClusters. After visual inspection of cluster assignments on UMAP, a resolution of 0.8 was deemed satisfactory for initial clustering.

For basic quality control, quality metrics including number of genes detected and percent of genes from the mitochondrial genome ("percent.mito") was visualized together with cluster assignment on UMAP, identifying a cluster of cells with high percent.mito which was removed. Cluster markers were then identified using Seurat::FindAllMarkers with the following parameters: assay = 'SCT', slot = 'scale.data', test.use = 't', and the 'features' parameter set to the top 3000 highly variable genes from SCTransform. Clusters were then assigned to major known brain cell types (excitatory neurons, inhibitory neurons, astrocytes, oligodendrocytes, oligodendrocyte precursor cells, microglia, endothelial cells, vascular cells) by inspection of cluster markers and by using cell type predictions generated by Azimuth (an online analysis platform for alignment of query single-cell datasets to annotated reference single-cell datasets), using the human primary motor cortex as the reference. A cluster with low mapping scores from Azimuth and lack of cell type-specific markers was removed. After all clusters have been assigned to major known brain cell types, separate seurat objects were created with only cells belonging to each cell type for subclustering analysis.

For subclustering of each cell type, data normalization, identification of high variable genes, dimensionality reduction, and clustering was repeated starting from the raw counts, again specifying a range of values for the resolution parameter for Seurat::FindClusters and using visual inspection of cluster separation on UMAP to select the optimal resolution parameter. Initial cluster markers were then identified using Seurat::FindAllMarkers with assay = 'SCT', slot = 'scale.data', test.use = 't' and filtered for adjusted *P* value < 0.05 (Bonferroni) and $\log_2$-fold change > 0.58. Cell type identity of clusters was then verified using Azimuth and inspection of cluster markers. In some cases, this process identified small clusters consisting of cells predicted to be another cell type by Azimuth, likely doublets, which were then removed. The remaining clusters were then assigned as bona fide cell type subclusters. Subcluster markers were then identified using Seurat::FindAllMarkers with the same parameters as above, and filtered for adjusted *P* value < 0.05 (Bonferonni). All cells removed during subclustering were also removed from the seurat object corresponding to overall dataset, which was then used for the analyses described below.

For inference of chr1q gain, the chr1q module score was generated using Seurat::AddModuleScore with assay = 'SCT' and the features parameter set to genes located on chr1q, which were identified using Ensembl Biomart and restricted to genes with official HGNC gene symbols. The chr1p module score was calculated similarly.

To identify chr1q gain-associated DEGs robust to cell type, an expression matrix consisting of Pearson residuals from SCTransform (the 'scale.data' slot of the 'SCT' assay) of genes that were detected in more than 5% of all cells was used as input to limma::lmFit (limma v3.56.2), using a model formula of the form '~ cell type + chr1q status'. Statistical shrinkage was then performed using limma:eBayes, with robust = 'TRUE'. DEGs were then filtered for adjusted *P* value < 0.05 (Benjamini-Hochberg) and $\log_2$-fold change > 0.32. To identify chr1q gain-associated DEGs for each cell type, Seurat::FindMarkers was used with the seurat object corresponding to each cell type, with assay = 'SCT', slot = 'scale.data', test.use = 't', ident.1 set to cells with chr1q module score > 0.25, and ident.2 set to cells with chr1q module score < 0.25. Since Seurat::FindMarkers uses Bonferonni correction by default, Benjamini-Hochberg adjusted *P* values were generated using p.adjust with method = 'fdr', and DEGs were filtered for adjusted *P* value < 0.95 and $\log_2$-fold change > 0.32. Given that when comparing cells with high chr1q

module score to those with low chr1q module score, genes on chr1q are more likely to be differentially expressed, we performed a secondary analysis where a more stringent *P* value adjustment (Bonferonni) was employed for genes on chr1q, which did not affect the number of DEGs recovered compared to using Benjamini-Hochberg adjustment for all genes.

Enrichment analysis of DEGs was performed for upregulated and downregulated DEGs separately using Enrichr (an online tool for gene set enrichment analysis), utilizing the R utility function enrichR::enrichr with the following gene set libraries: "ENCODE_and_ChEA_Consensus_TFs_from_ChIP-X', 'ARCHS4_TFs_Coexp', 'Reactome_2022', 'ARCHS4_Kinases_Coexp', 'GO_Biological_Process_2023', and 'GO_Cellular_Component_2023'. The ENCODE and ChEA consensus library consist of gene sets associated with transcriptional regulators through ChIP-seq experiments. ARCHS4 is a continually updated compendium of all published RNA-seq datasets re-processed through a common pipeline enabling co-expression analysis of genes with known transcription factors (TFs) and kinases. The adjusted *P* values from Enrichr are used for the plots in Fig. S4-6, which show only terms with adjusted *P* value < 0.1.

For network visualization of genes shown in Fig. 2h and Fig. 3c, genes of interest were used as the input to the STRING (v11.5) app's "protein query" function in CytoScape (v3.10.0); a minimum cutoff of 0.6 was used for the confidence score, which reflects the degree of certainty regarding the existence of a regulatory relationship between two proteins based on current evidence. Genes without annotated functions in their NCBI gene summary were not included for visualization.

Statistics

The Pearson's Chi-square test was performed with the function 'chisq.test' in R with default parameters.

SUPPLEMENTAL FIGURE LEGENDS

Fig. S1 | Additional histology of hyaline protoplasmic astrocytopathy. H&E staining of cortex from resected brain tissue at age 3 years at 40x (left) and 400x (right) original magnification. The histologic sections reveal brightly eosinophilic, refractile (glassy) inclusions within the cell bodies of glial cells, predominantly those with the morphological appearance of the so-called “protoplasmic astrocytes”. These glial cells were scattered throughout the cortex as also appeared as perineuronal satellite cells. The inclusions were predominantly within the glial cells, but also occurred as small neuropil deposits as well as in perivascular spaces. The inclusions attained various shapes, occasionally reminiscent of Rosenthal fibers, but with more distinctive hyalinized (glassy) appearance. These inclusions were widely dispersed throughout all cortical sections examined but were not identified within the white matter. Immunohistochemical studies revealed diffuse cortical and white matter gliosis as demonstrated with the GFAP stains (not shown here). Neuronal stains MAP2, Synaptophysin and NeuN (not shown here) demonstrated an apparent increase in the number of neuronal cells within the white matter, without clear evidence of focal cortical dysplasia.

Fig. S2 | Appropriate expression of cell-type specific markers and expected variation in median number of genes detected seen on quality-control analysis. a, Heatmap of the top 10 cell type-specific genes across all major cell types captured by snRNA-seq. **b**, UMAP of all cells recovered from snRNA-seq colored by cluster assignment, median number of genes detected, or percent of genes from the mitochondrial genome.

Fig. S3 | Subpopulations of OPCs, microglia, endothelial cells, and vascular cells seen on subclustering of cell types without inferred chr1q gain; low median number of genes detected in Ast.s4 seen on subclustering of astrocytes. a, UMAP of cell types without inferred chr1q gain colored by subcluster assignment or chr1q module score. **b**, UMAP of astrocytes colored by subcluster assignment, median number of genes detected, or percent of genes from the mitochondrial genome. The low median number of genes detected in Ast.s4 makes it unlikely that Ast.s4 corresponds to astrocyte-neuron doublets, which tend to have >2000 median number of genes detected and were removed during quality control.

Fig. S4 | Cell type-robust and cell type-specific chr1q gain-associated DEGs. Volcano plots of chr1q gain associated DEGs robust to cell type (**a**), in excitatory neurons (**b**), inhibitory neurons (**c**), or astrocytes (**d**). DEGs shared among excitatory neurons, inhibitory neurons, and astrocytes are marked in panel **a**; DEGs specific to excitatory neurons, inhibitory neurons, or astrocytes are marked in panels **b**, **c**, and **d**, respectively.

Fig. S5 | Enrichment analysis of DEGs associated with chr1q gain robust to cell type. See Detailed Methods for details regarding the gene set libraries included for analysis. Only terms with adjusted *P* value < 0.1 are shown.

Fig. S6 | Enrichment analysis of DEGs associated with chr1q gain in excitatory neurons. See Detailed Methods for details regarding the gene set libraries included for analysis. Only terms with adjusted *P* value < 0.1 are shown.

Fig. S7 | Enrichment analysis of DEGs associated with chr1q gain in inhibitory neurons. See Detailed Methods for details regarding the gene set libraries included for analysis. Only terms with adjusted *P* value < 0.1 are shown.

Fig. S8 | Enrichment analysis of DEGs associated with chr1q gain in astrocytes. See Detailed Methods for details regarding the gene set libraries included for analysis. Only terms with adjusted *P* value < 0.1 are shown.

Fig. S9 | Enrichment analysis of DEGs in Exc.s6 compared to all other excitatory neurons. See Detailed Methods for details regarding the gene set libraries included for analysis. Only terms with adjusted *P* value < 0.1 are shown.

Fig. S10 | Enrichment analysis of DEGs in Ast.s3 compared to all other astrocytes. See Detailed Methods for details regarding the gene set libraries included for analysis. Only terms with adjusted *P* value < 0.1 are shown.

Fig. S11 | Enrichment analysis of DEGs in Ast.s4 compared to all other astrocytes. See Detailed Methods for details regarding the gene set libraries included for analysis. Only terms with adjusted *P* value < 0.1 are shown.

SUPPLEMENTAL TABLES LEGENDS

Table S1 | Chr1q gain associated DEGs robust to cell type or in excitatory neurons, inhibitory neurons, and astrocytes. Chr1q gain associated DEGs robust to cell type were identified using limma (see Detailed Methods) whereas chr1q gain associated DEGs in excitatory neurons, inhibitory neurons, and astrocytes were identified using Seurat::FindMarkers (see Detailed Methods). Column names in the first tab: 'gene' - HGNC gene symbol of the DEG, 'logFC' - average $\log_2$-fold change, 'AveExpr' - average log-scaled expression score of the DEG (see Detailed Methods), 't' - value of t statistic from limma, 'P.Value' - unadjusted *P* value from limma, 'adj.P.Val' - Benjamini-Hochberg adjusted *P* value. Column names in remaining tabs: 'gene' - HGNC gene symbol of the DEG, 'p_val' - unadjusted *P* value, 'avg_diff' - average $\log_2$-fold change, 'pct.1' - percent of cells with chr1q gain in which the DEG was detected, 'pct.2' - percent of cells without chr1q gain in which the DEG was detected, 'p_val_adj' - Benjamini-Hochberg adjusted *P* value.

Table S2 | Enrichment analysis of chr1q gain associated DEGs robust to cell type or in excitatory neurons, inhibitory neurons, and astrocytes. Enrichment analysis was performed separately on upregulated DEGs and downregulated DEGs. Column names: 'Library' - gene set library, 'Term' - name of the gene set within the gene set library, 'Overlap' - number of DEGs overlapping with the gene set over the number of genes within the gene set, 'P.value' - unadjusted *P* value from Fisher's exact test, 'Odds.Ratio' - odds ratio from Fisher's exact test, 'Genes' - the DEGs overlapping with the gene set, 'Combined.Score' - a score that combines the odds ratio and *P* value, 'DE_direction' - the direction of differential expression of the DEGs.

Table S3 | Excitatory neuron, inhibitory neuron, and astrocyte subcluster DEGs. Column names: 'gene' - HGNC gene symbol of the DEG, 'p_val' - unadjusted *P* value, 'avg_diff' - average $\log_2$-fold change, 'pct.1' - percent of cells in the subcluster of interest in which the DEG was detected, 'pct.2' - percent of cells not in the subcluster of interest in which the DEG was detected, 'p_val_adj' - Benjamini-Hochberg adjusted *P* value, 'cluster' - the subcluster of interest.

Table S4 | Enrichment analysis of excitatory neuron, inhibitory neuron, and astrocyte subcluster DEGs. Enrichment analysis was performed separately on upregulated DEGs and downregulated DEGs. Column names: 'Library' - gene set library, 'Term' - name of the gene set within the gene set library, 'Overlap' - number of DEGs overlapping with the gene set over the number of genes within the gene set, 'P.value' - unadjusted *P* value from Fisher's exact test, 'Odds.Ratio' - odds ratio from Fisher's exact test, 'Genes' - the DEGs overlapping with the gene set, 'Combined.Score' - a score that combines the odds ratio and *P* value, 'DE_direction' - the direction of differential expression of the DEGs.

Fig. 1

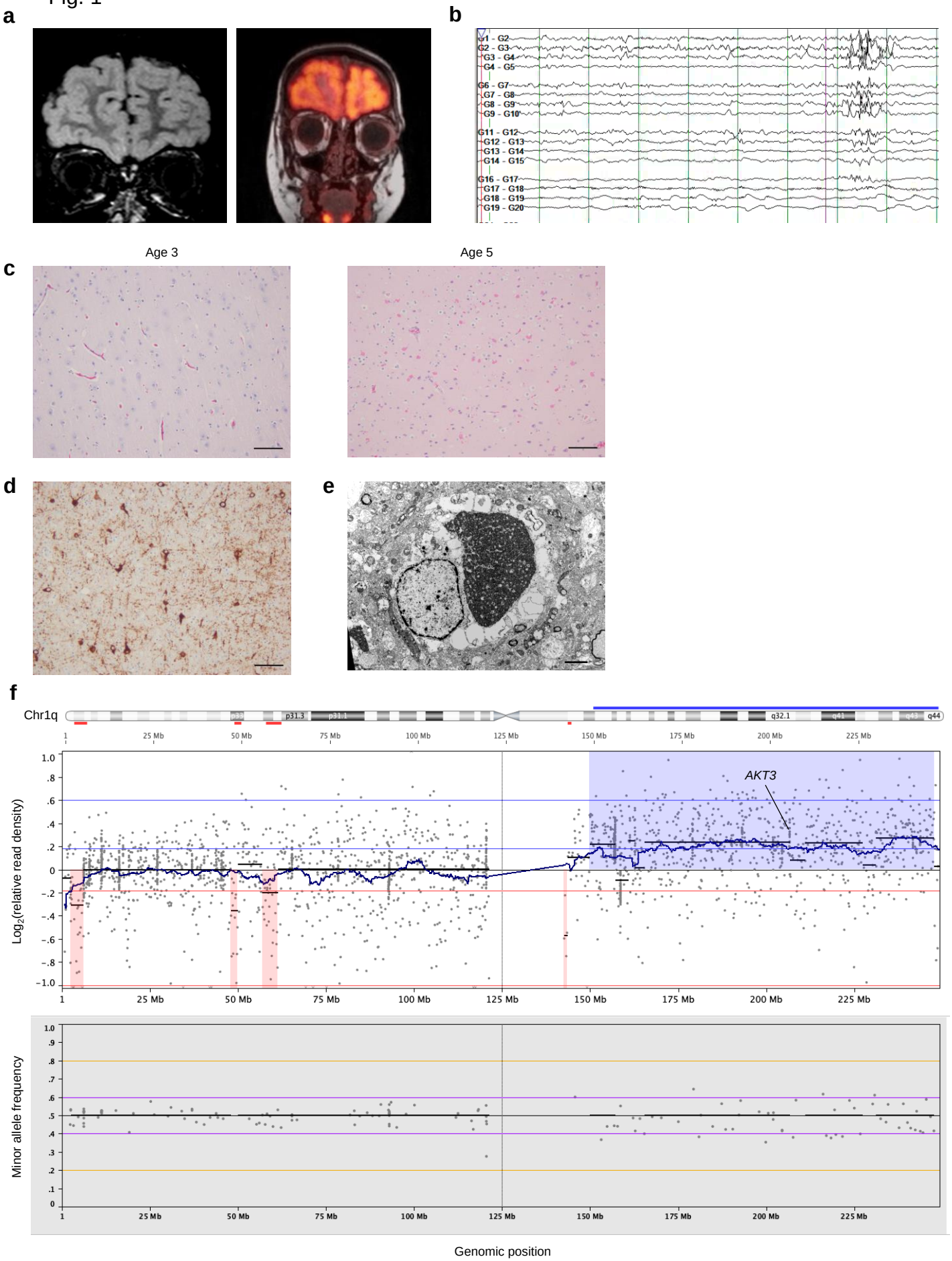
a
b
G1 - G2
G2 - G3
G3 - G4
G4 - G5
G6 - G7
G7 - G8
G8 - G9
G9 - G10
G11 - G12
G12 - G13
G13 - G14
G14 - G15
G16 - G17
G17 - G18
G18 - G19
G19 - G20
Age 3
Age 5
c
d
e
f
Chr1q
p31.3
p31.1
q32.1
q41
q44
1
25 Mb
50 Mb
75 Mb
100 Mb
125 Mb
150 Mb
175 Mb
200 Mb
225 Mb
AKT3
Log2(relative read density)
1.0
.8
.6
.4
.2
0
-.2
-.4
-.6
-.8
-1.0
Minor allele frequency
.9
.7
.5
.3
.1
Genomic position

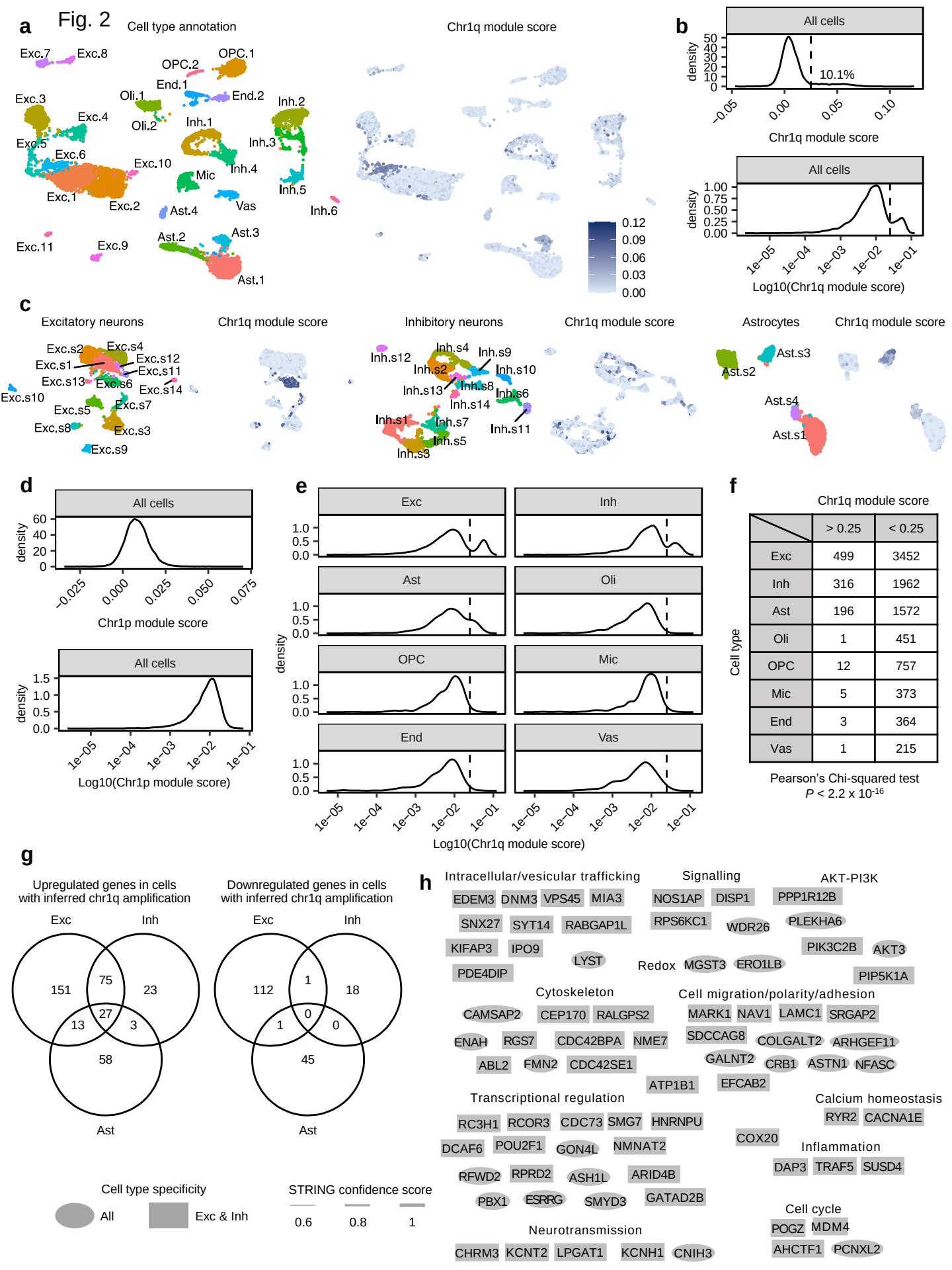
Fig. 2
a
Cell type annotation
Exc.7
Exc.8
OPC.2
OPC.1
End.1
Oli.1
End.2
Exc.3
Inh.2
Exc.4
Oli.2
Inh.1
Exc.5
Inh.3
Exc.6
Exc.10
Inh.4
Mic
Exc.1
Inh.5
Exc.2
Ast.4
Vas
Inh.6
Exc.11
Exc.9
Ast.2
Ast.3
Ast.1
Chr1q module score
0.12
0.09
0.06
0.03
0.00
b
All cells
density
10.1%
Chr1q module score
Log10(Chr1q module score)
c
Excitatory neurons
Chr1q module score
Inhibitory neurons
Astrocytes
Exc.s2
Exc.s4
Exc.s1
Exc.s12
Exc.s11
Exc.s13
Exc.s6
Exc.s14
Exc.s10
Exc.s5
Exc.s7
Exc.s8
Exc.s3
Exc.s9
Inh.s12
Inh.s4
Inh.s9
Inh.s2
Inh.s10
Inh.s13
Inh.s8
Inh.s6
Inh.s14
Inh.s1
Inh.s7
Inh.s11
Inh.s5
Inh.s3
Ast.s3
Ast.s2
Ast.s4
Ast.s1
d
All cells
density
Chr1p module score
Log10(Chr1p module score)
e
Exc
Inh
Ast
Oli
OPC
Mic
End
Vas
density
Log10(Chr1q module score)
f
Chr1q module score
Cell type
> 0.25
< 0.25
Exc 499 3452
Inh 316 1962
Ast 196 1572
Oli 1 451
OPC 12 757
Mic 5 373
End 3 364
Vas 1 215
Pearson's Chi-squared test
P < 2.2 x 10-16
g
Upregulated genes in cells with inferred chr1q amplification
Exc
Inh
151
75
23
27
13
3
58
Ast
Downregulated genes in cells with inferred chr1q amplification
112
1
18
0
1
0
45
Cell type specificity
All
Exc & Inh
STRING confidence score
0.6
0.8
1
h
Intracellular/vesicular trafficking
EDEM3
DNM3
VPS45
MIA3
SNX27
SYT14
RABGAP1L
KIFAP3
IPO9
LYST
PDE4DIP
Signalling
NOS1AP
DISP1
RPS6KC1
WDR26
AKT-PI3K
PPP1R12B
PLEKHA6
PIK3C2B
AKT3
Redox
MGST3
ERO1LB
PIP5K1A
Cytoskeleton
CAMSAP2
CEP170
RALGPS2
ENAH
RGS7
CDC42BPA
NME7
ABL2
FMN2
CDC42SE1
Cell migration/polarity/adhesion
MARK1
NAV1
LAMC1
SRGAP2
SDCCAG8
COLGALT2
ARHGEF11
GALNT2
CRB1
ASTN1
NFASC
EFCAB2
ATP1B1
Transcriptional regulation
RC3H1
RCOR3
CDC73
SMG7
HNRNPU
DCAF6
POU2F1
GON4L
NMNAT2
RFWD2
RPRD2
ASH1L
ARID4B
PBX1
ESRRG
SMYD3
GATAD2B
Calcium homeostasis
RYR2
CACNA1E
COX20
Inflammation
DAP3
TRAF5
SUSD4
Cell cycle
POGZ
MDM4
AHCTF1
PCNXL2
Neurotransmission
CHRM3
KCNT2
LPGAT1
KCNH1
CNIH3

Fig. 3

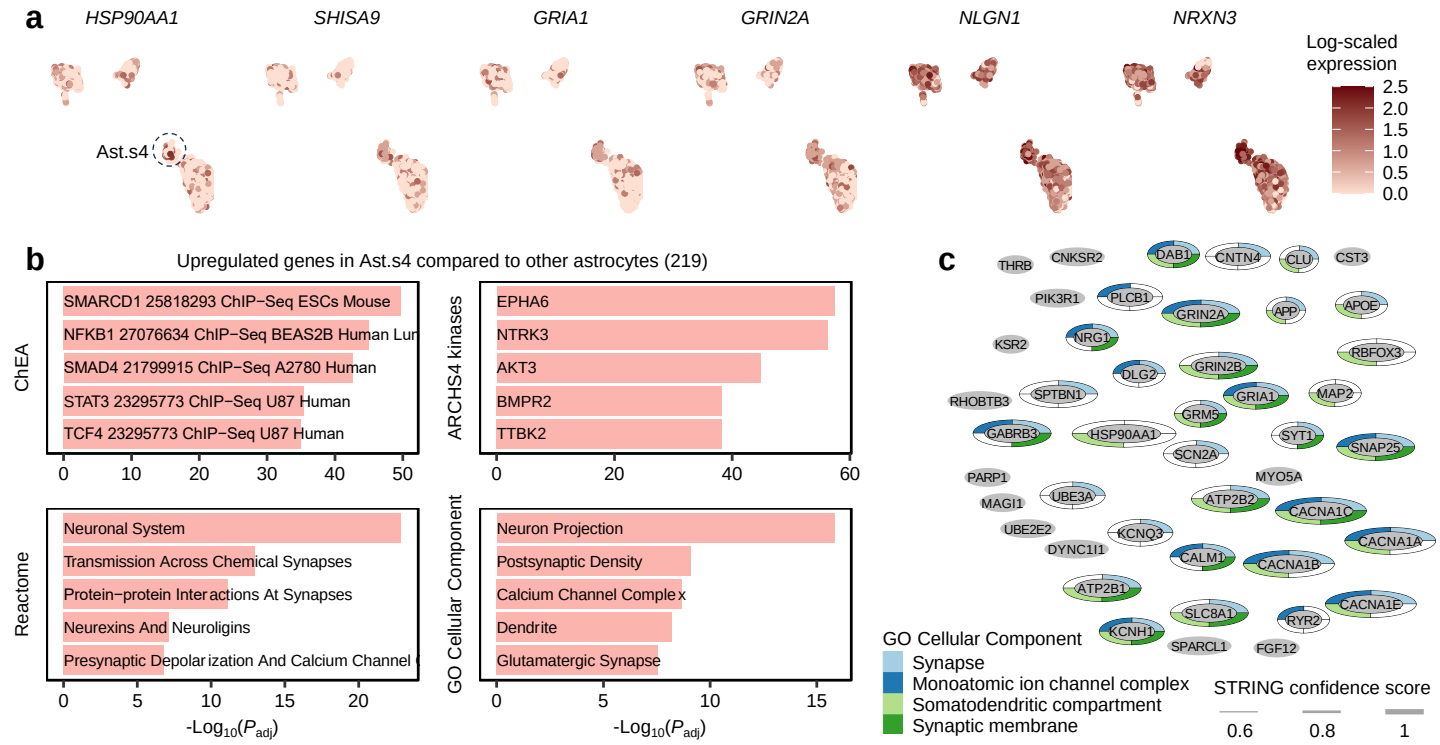
a
HSP90AA1
SHISA9
GRIA1
GRIN2A
NLGN1
NRXN3
Ast.s4
Log-scaled expression
2.5
2.0
1.5
1.0
0.5
0.0
b
Upregulated genes in Ast.s4 compared to other astrocytes (219)
ChEA
SMARCD1 25818293 ChIP−Seq ESCs Mouse
NFKB1 27076634 ChIP−Seq BEAS2B Human Lun
SMAD4 21799915 ChIP−Seq A2780 Human
STAT3 23295773 ChIP−Seq U87 Human
TCF4 23295773 ChIP−Seq U87 Human
0 10 20 30 40 50
ARCHS4 kinases
EPHA6
NTRK3
AKT3
BMPR2
TTBK2
0 20 40 60
Reactome
Neuronal System
Transmission Across Chemical Synapses
Protein−protein Interactions At Synapses
Neurexins And Neuroligins
Presynaptic Depolarization And Calcium Channel
0 5 10 15 20
-Log10(Padj)
GO Cellular Component
Neuron Projection
Postsynaptic Density
Calcium Channel Complex
Dendrite
Glutamatergic Synapse
0 5 10 15
-Log10(Padj)
c
THRB
CNKSR2
DAB1
CNTN4
CLU
CST3
PIK3R1
PLCB1
GRIN2A
APP
APOE
KSR2
NRG1
RBFOX3
DLG2
GRIN2B
RHOBTB3
SPTBN1
GRIA1
MAP2
GRM5
GABRB3
HSP90AA1
SYT1
SNAP25
SCN2A
PARP1
MYO5A
MAGI1
UBE3A
ATP2B2
CACNA1C
UBE2E2
KCNQ3
CACNA1A
DYNC1I1
CALM1
CACNA1B
ATP2B1
CACNA1E
SLC8A1
RYR2
KCNH1
SPARCL1
FGF12
GO Cellular Component
Synapse
Monoatomic ion channel complex
Somatodendritic compartment
Synaptic membrane
STRING confidence score
0.6
0.8
1

Fig. S1

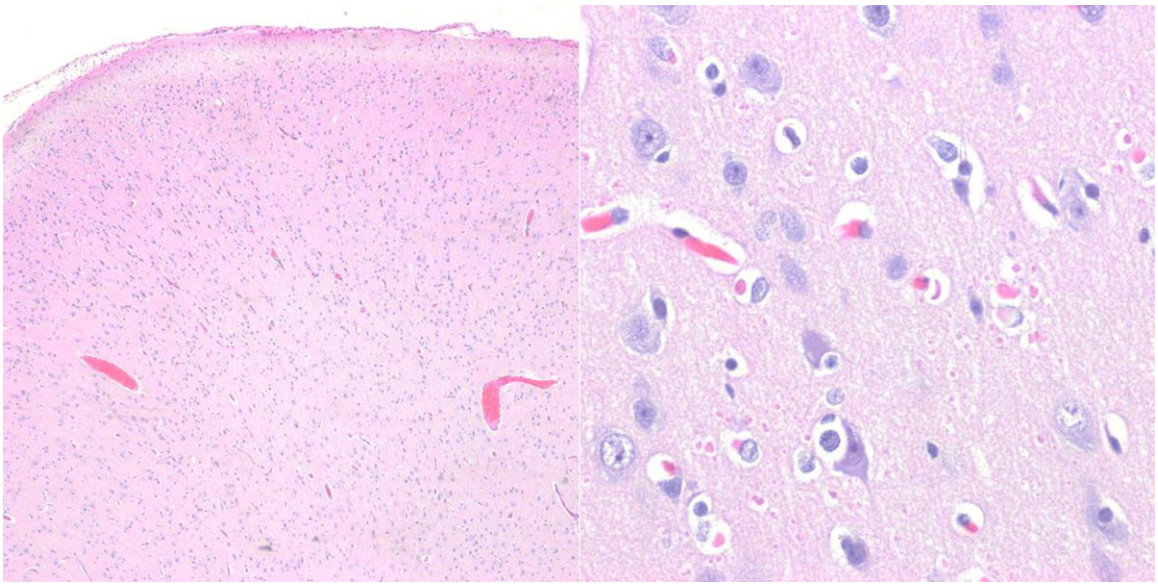

Fig. S2

a

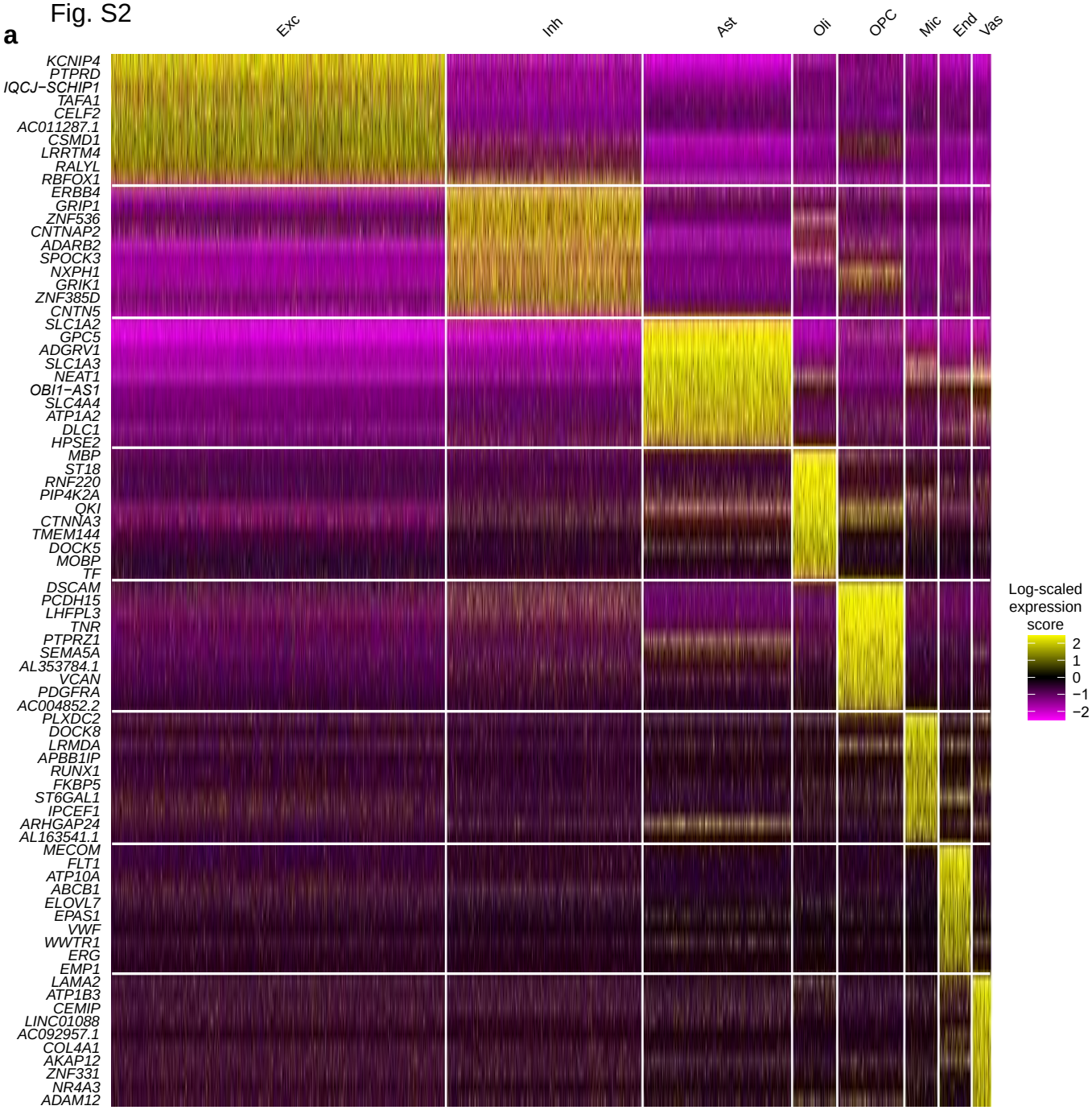
Exc
Inh
Ast
Oli
OPC
Mic
End
Vas
KCNIP4
PTPRD
IQCJ−SCHIP1
TAFA1
CELF2
AC011287.1
CSMD1
LRRTM4
RALYL
RBFOX1
ERBB4
GRIP1
ZNF536
CNTNAP2
ADARB2
SPOCK3
NXPH1
GRIK1
ZNF385D
CNTN5
SLC1A2
GPC5
ADGRV1
SLC1A3
NEAT1
OBI1−AS1
SLC4A4
ATP1A2
DLC1
HPSE2
MBP
ST18
RNF220
PIP4K2A
QKI
CTNNA3
TMEM144
DOCK5
MOBP
TF
DSCAM
PCDH15
LHFPL3
TNR
PTPRZ1
SEMA5A
AL353784.1
VCAN
PDGFRA
AC004852.2
PLXDC2
DOCK8
LRMDA
APBB1IP
RUNX1
FKBP5
ST6GAL1
IPCEF1
ARHGAP24
AL163541.1
MECOM
FLT1
ATP10A
ABCB1
ELOVL7
EPAS1
VWF
WWTR1
ERG
EMP1
LAMA2
ATP1B3
CEMIP
LINC01088
AC092957.1
COL4A1
AKAP12
ZNF331
NR4A3
ADAM12
Log-scaled expression score
2
1
0
−1
−2

b

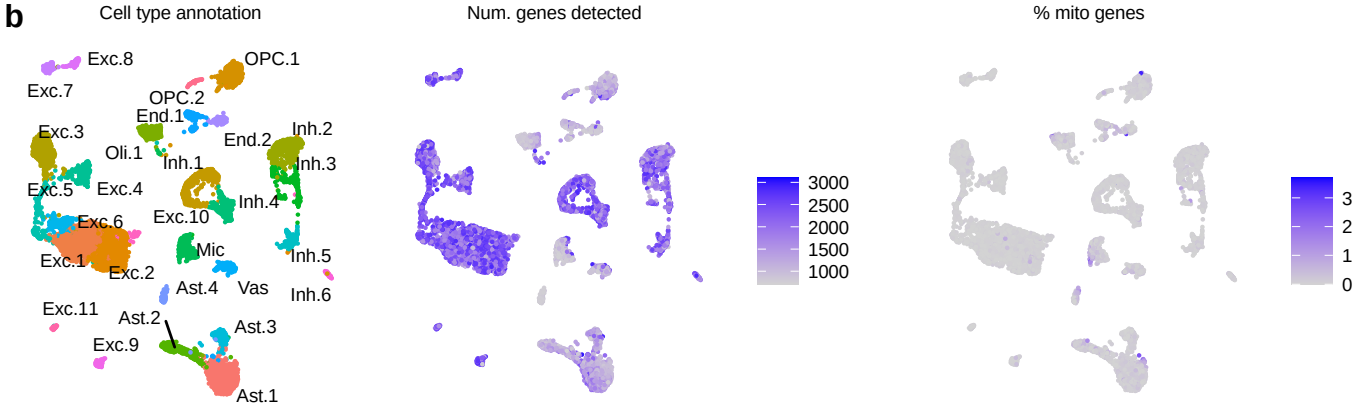
Cell type annotation
Num. genes detected
% mito genes
Exc.8
OPC.1
Exc.7
OPC.2
End.1
Exc.3
Inh.2
End.2
Oli.1
Inh.1
Inh.3
Exc.5
Exc.4
Inh.4
Exc.10
Exc.6
Mic
Inh.5
Exc.1
Exc.2
Ast.4
Vas
Inh.6
Exc.11
Ast.2
Ast.3
Exc.9
Ast.1
3000
2500
2000
1500
1000
3
2
1
0

Fig. S3

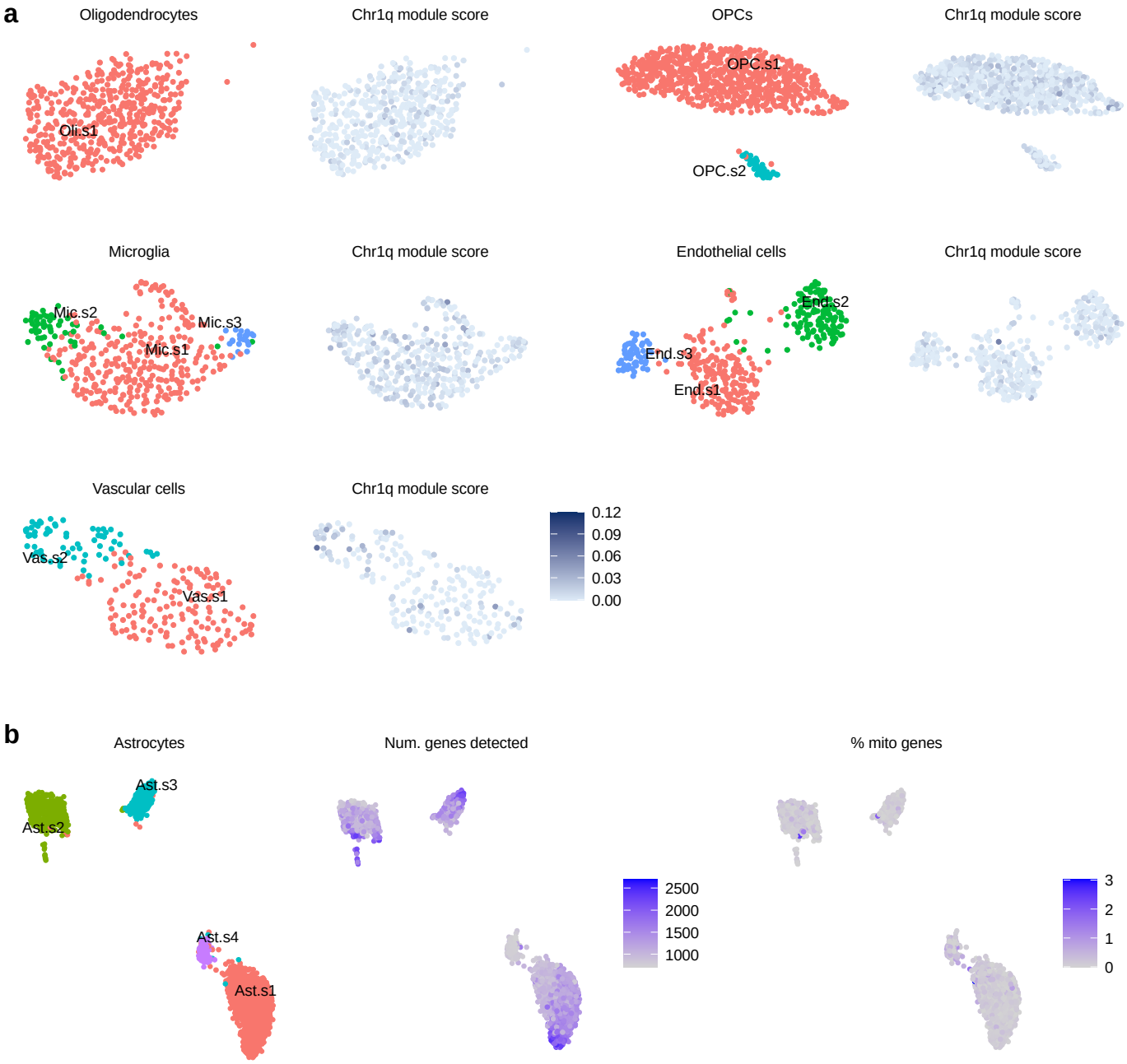
a
Oligodendrocytes
Oli.s1
Chr1q module score
OPCs
OPC.s1
OPC.s2
Chr1q module score
Microglia
Mic.s2
Mic.s3
Mic.s1
Chr1q module score
Endothelial cells
End.s2
End.s3
End.s1
Chr1q module score
Vascular cells
Vas.s2
Vas.s1
Chr1q module score
0.12
0.09
0.06
0.03
0.00
b
Astrocytes
Ast.s3
Ast.s2
Ast.s4
Ast.s1
Num. genes detected
2500
2000
1500
1000
% mito genes
3
2
1
0

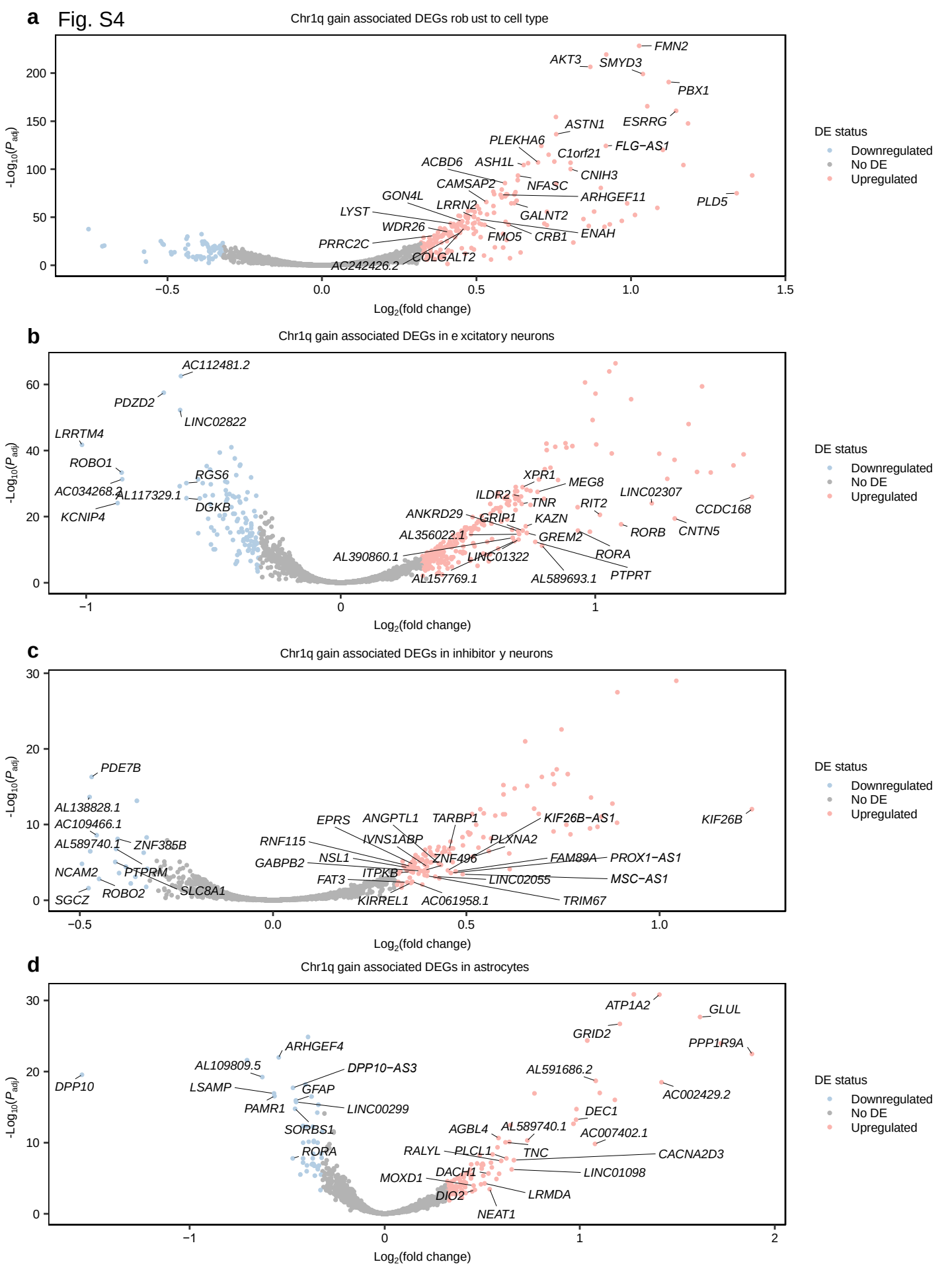
a
Fig. S4
Chr1q gain associated DEGs rob ust to cell type
FMN2
AKT3
SMYD3
PBX1
ASTN1
ESRRG
PLEKHA6
FLG−AS1
C1orf21
ACBD6
ASH1L
CNIH3
CAMSAP2
NFASC
GON4L
ARHGEF11
PLD5
LYST
LRRN2
GALNT2
WDR26
FMO5
CRB1
ENAH
PRRC2C
COLGALT2
AC242426.2
-Log10(Padj)
Log2(fold change)
DE status
Downregulated
No DE
Upregulated
b
Chr1q gain associated DEGs in e xcitatory neurons
AC112481.2
PDZD2
LINC02822
LRRTM4
ROBO1
RGS6
AC034268.2
AL117329.1
DGKB
KCNIP4
XPR1
MEG8
ILDR2
TNR
LINC02307
RIT2
CCDC168
ANKRD29
GRIP1
KAZN
RORB
CNTN5
AL356022.1
GREM2
AL390860.1
LINC01322
RORA
AL157769.1
AL589693.1
PTPRT
c
Chr1q gain associated DEGs in inhibitor y neurons
PDE7B
AL138828.1
AC109466.1
AL589740.1
ZNF385B
NCAM2
PTPRM
SGCZ
ROBO2
SLC8A1
EPRS
ANGPTL1
TARBP1
KIF26B−AS1
KIF26B
RNF115
IVNS1ABP
PLXNA2
GABPB2
NSL1
ZNF496
FAM89A
PROX1−AS1
FAT3
ITPKB
LINC02055
MSC−AS1
KIRREL1
AC061958.1
TRIM67
d
Chr1q gain associated DEGs in astrocytes
ATP1A2
GLUL
GRID2
PPP1R9A
ARHGEF4
AL109809.5
DPP10−AS3
DPP10
LSAMP
GFAP
PAMR1
LINC00299
AL591686.2
AC002429.2
DEC1
SORBS1
AGBL4
AL589740.1
AC007402.1
RORA
RALYL
PLCL1
TNC
CACNA2D3
MOXD1
DACH1
LINC01098
DIO2
LRMDA
NEAT1

Fig. S5

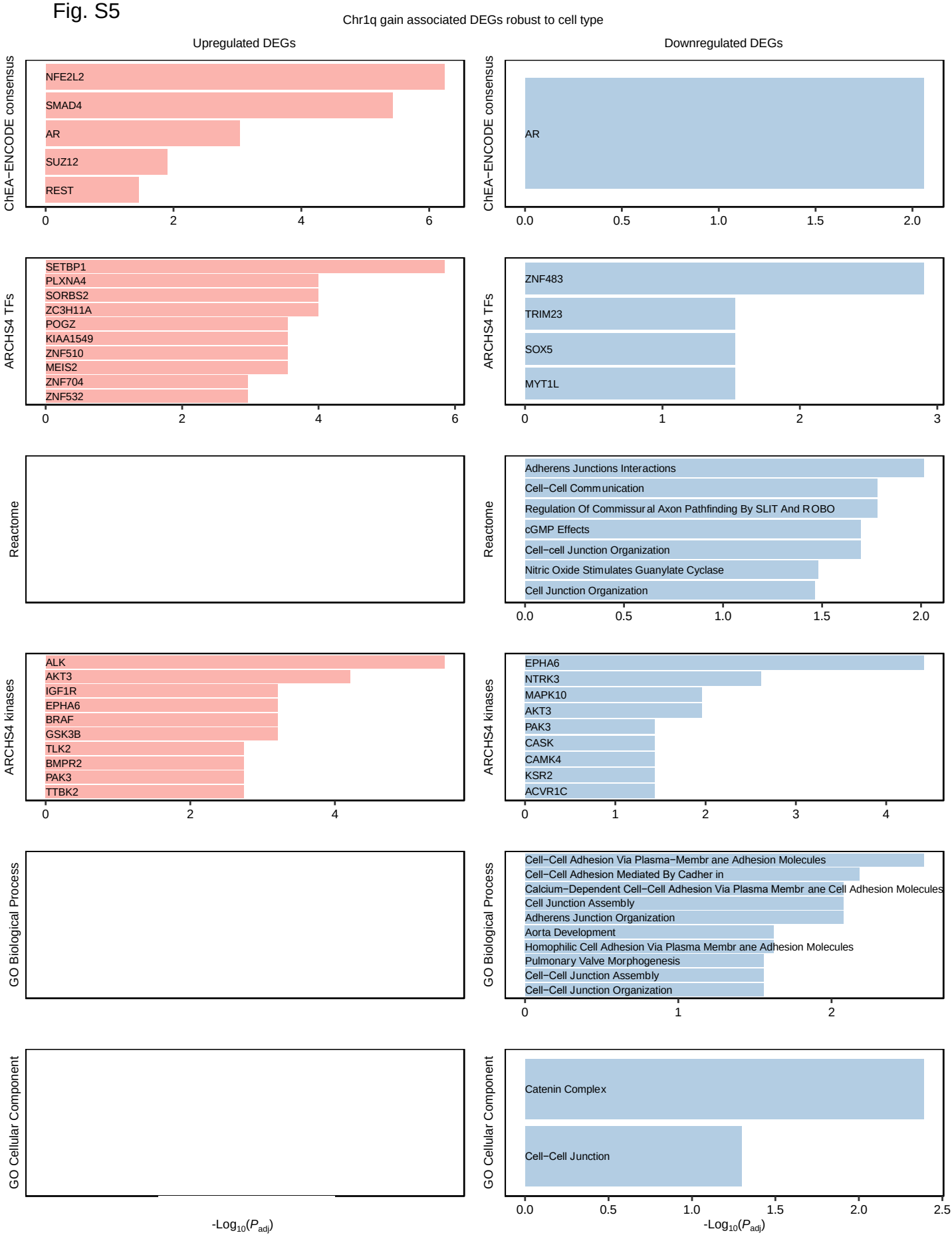
Chr1q gain associated DEGs robust to cell type
Upregulated DEGs
Downregulated DEGs
ChEA−ENCODE consensus
NFE2L2
SMAD4
AR
SUZ12
REST
0
2
4
6
ChEA−ENCODE consensus
AR
0.0
0.5
1.0
1.5
2.0
ARCHS4 TFs
SETBP1
PLXNA4
SORBS2
ZC3H11A
POGZ
KIAA1549
ZNF510
MEIS2
ZNF704
ZNF532
0
2
4
6
ARCHS4 TFs
ZNF483
TRIM23
SOX5
MYT1L
0
1
2
3
Reactome
Reactome
Adherens Junctions Interactions
Cell−Cell Communication
Regulation Of Commissural Axon Pathfinding By SLIT And ROBO
cGMP Effects
Cell−cell Junction Organization
Nitric Oxide Stimulates Guanylate Cyclase
Cell Junction Organization
0.0
0.5
1.0
1.5
2.0
ARCHS4 kinases
ALK
AKT3
IGF1R
EPHA6
BRAF
GSK3B
TLK2
BMPR2
PAK3
TTBK2
0
2
4
ARCHS4 kinases
EPHA6
NTRK3
MAPK10
AKT3
PAK3
CASK
CAMK4
KSR2
ACVR1C
0
1
2
3
4
GO Biological Process
GO Biological Process
Cell−Cell Adhesion Via Plasma−Membr ane Adhesion Molecules
Cell−Cell Adhesion Mediated By Cadher in
Calcium−Dependent Cell−Cell Adhesion Via Plasma Membr ane Cell Adhesion Molecules
Cell Junction Assembly
Adherens Junction Organization
Aorta Development
Homophilic Cell Adhesion Via Plasma Membr ane Adhesion Molecules
Pulmonary Valve Morphogenesis
Cell−Cell Junction Assembly
Cell−Cell Junction Organization
0
1
2
GO Cellular Component
GO Cellular Component
Catenin Complex
Cell−Cell Junction
0.0
0.5
1.0
1.5
2.0
2.5
-Log10(Padj)
-Log10(Padj)

Fig. S6

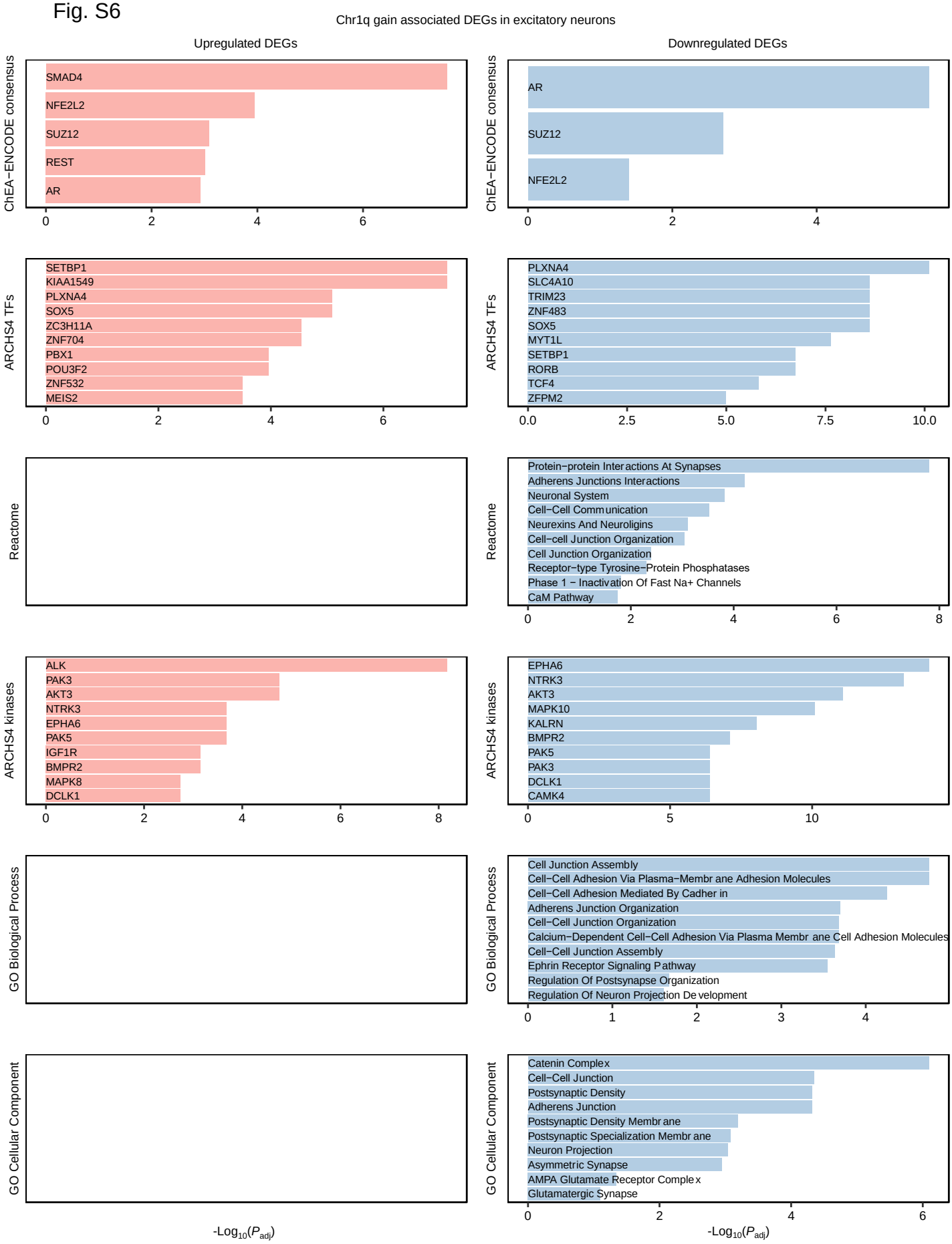
Chr1q gain associated DEGs in excitatory neurons
Upregulated DEGs
Downregulated DEGs
ChEA−ENCODE consensus
SMAD4
NFE2L2
SUZ12
REST
AR
0
2
4
6
ChEA−ENCODE consensus
AR
SUZ12
NFE2L2
0
2
4
ARCHS4 TFs
SETBP1
KIAA1549
PLXNA4
SOX5
ZC3H11A
ZNF704
PBX1
POU3F2
ZNF532
MEIS2
0
2
4
6
ARCHS4 TFs
PLXNA4
SLC4A10
TRIM23
ZNF483
SOX5
MYT1L
SETBP1
RORB
TCF4
ZFPM2
0.0
2.5
5.0
7.5
10.0
Reactome
Reactome
Protein−protein Interactions At Synapses
Adherens Junctions Interactions
Neuronal System
Cell−Cell Communication
Neurexins And Neuroligins
Cell−cell Junction Organization
Cell Junction Organization
Receptor−type Tyrosine−Protein Phosphatases
Phase 1 − Inactivation Of Fast Na+ Channels
CaM Pathway
0
2
4
6
8
ARCHS4 kinases
ALK
PAK3
AKT3
NTRK3
EPHA6
PAK5
IGF1R
BMPR2
MAPK8
DCLK1
0
2
4
6
8
ARCHS4 kinases
EPHA6
NTRK3
AKT3
MAPK10
KALRN
BMPR2
PAK5
PAK3
DCLK1
CAMK4
0
5
10
GO Biological Process
GO Biological Process
Cell Junction Assembly
Cell−Cell Adhesion Via Plasma−Membrane Adhesion Molecules
Cell−Cell Adhesion Mediated By Cadherin
Adherens Junction Organization
Cell−Cell Junction Organization
Calcium−Dependent Cell−Cell Adhesion Via Plasma Membrane Cell Adhesion Molecules
Cell−Cell Junction Assembly
Ephrin Receptor Signaling Pathway
Regulation Of Postsynapse Organization
Regulation Of Neuron Projection Development
0
1
2
3
4
GO Cellular Component
GO Cellular Component
Catenin Complex
Cell−Cell Junction
Postsynaptic Density
Adherens Junction
Postsynaptic Density Membrane
Postsynaptic Specialization Membrane
Neuron Projection
Asymmetric Synapse
AMPA Glutamate Receptor Complex
Glutamatergic Synapse
0
2
4
6
-Log10(Padj)
-Log10(Padj)

Fig. S7

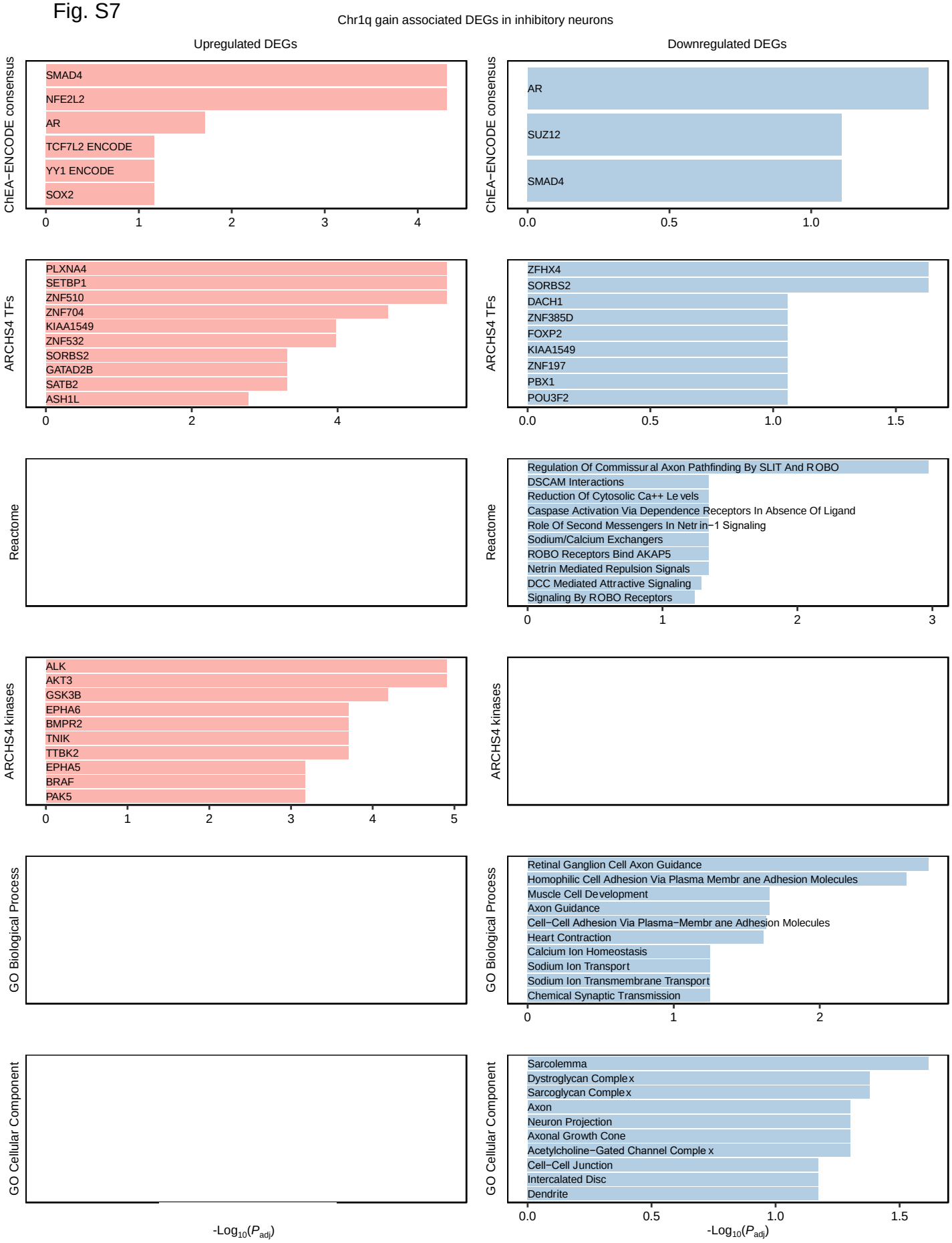
Chr1q gain associated DEGs in inhibitory neurons
Upregulated DEGs
Downregulated DEGs
ChEA−ENCODE consensus
SMAD4
NFE2L2
AR
TCF7L2 ENCODE
YY1 ENCODE
SOX2
0
1
2
3
4
ChEA−ENCODE consensus
AR
SUZ12
SMAD4
0.0
0.5
1.0
ARCHS4 TFs
PLXNA4
SETBP1
ZNF510
ZNF704
KIAA1549
ZNF532
SORBS2
GATAD2B
SATB2
ASH1L
0
2
4
ARCHS4 TFs
ZFHX4
SORBS2
DACH1
ZNF385D
FOXP2
KIAA1549
ZNF197
PBX1
POU3F2
0.0
0.5
1.0
1.5
Reactome
Reactome
Regulation Of Commissural Axon Pathfinding By SLIT And ROBO
DSCAM Interactions
Reduction Of Cytosolic Ca++ Levels
Caspase Activation Via Dependence Receptors In Absence Of Ligand
Role Of Second Messengers In Netrin−1 Signaling
Sodium/Calcium Exchangers
ROBO Receptors Bind AKAP5
Netrin Mediated Repulsion Signals
DCC Mediated Attractive Signaling
Signaling By ROBO Receptors
0
1
2
3
ARCHS4 kinases
ALK
AKT3
GSK3B
EPHA6
BMPR2
TNIK
TTBK2
EPHA5
BRAF
PAK5
0
1
2
3
4
5
ARCHS4 kinases
GO Biological Process
GO Biological Process
Retinal Ganglion Cell Axon Guidance
Homophilic Cell Adhesion Via Plasma Membrane Adhesion Molecules
Muscle Cell Development
Axon Guidance
Cell−Cell Adhesion Via Plasma−Membrane Adhesion Molecules
Heart Contraction
Calcium Ion Homeostasis
Sodium Ion Transport
Sodium Ion Transmembrane Transport
Chemical Synaptic Transmission
0
1
2
GO Cellular Component
GO Cellular Component
Sarcolemma
Dystroglycan Complex
Sarcoglycan Complex
Axon
Neuron Projection
Axonal Growth Cone
Acetylcholine−Gated Channel Complex
Cell−Cell Junction
Intercalated Disc
Dendrite
0.0
0.5
1.0
1.5
-Log10(Padj)
-Log10(Padj)

Fig. S8

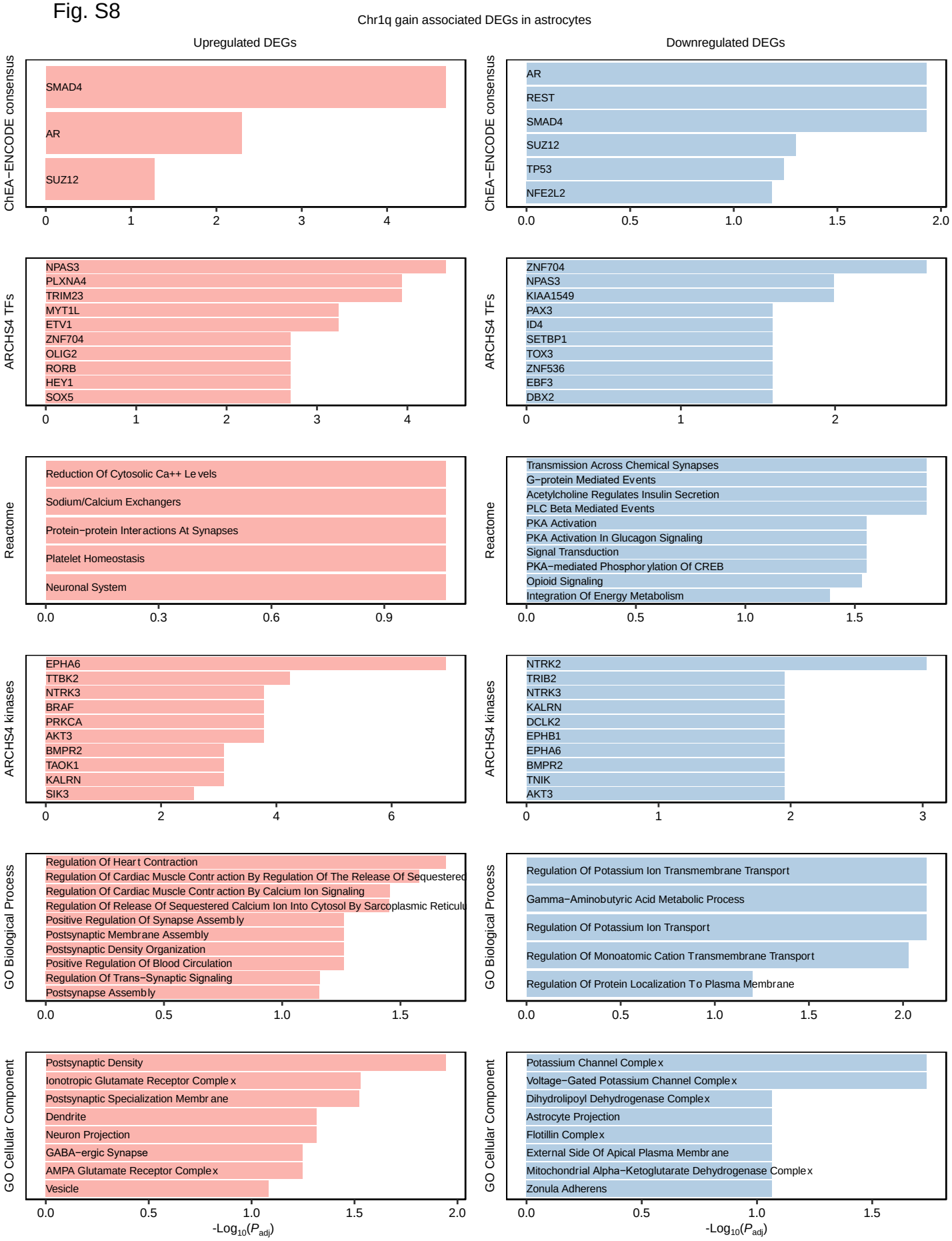
Chr1q gain associated DEGs in astrocytes
Upregulated DEGs
Downregulated DEGs
ChEA−ENCODE consensus
SMAD4
AR
SUZ12
0
1
2
3
4
ChEA−ENCODE consensus
AR
REST
SMAD4
SUZ12
TP53
NFE2L2
0.0
0.5
1.0
1.5
2.0
ARCHS4 TFs
NPAS3
PLXNA4
TRIM23
MYT1L
ETV1
ZNF704
OLIG2
RORB
HEY1
SOX5
0
1
2
3
4
ARCHS4 TFs
ZNF704
NPAS3
KIAA1549
PAX3
ID4
SETBP1
TOX3
ZNF536
EBF3
DBX2
0
1
2
Reactome
Reduction Of Cytosolic Ca++ Levels
Sodium/Calcium Exchangers
Protein−protein Interactions At Synapses
Platelet Homeostasis
Neuronal System
0.0
0.3
0.6
0.9
Reactome
Transmission Across Chemical Synapses
G−protein Mediated Events
Acetylcholine Regulates Insulin Secretion
PLC Beta Mediated Events
PKA Activation
PKA Activation In Glucagon Signaling
Signal Transduction
PKA−mediated Phosphorylation Of CREB
Opioid Signaling
Integration Of Energy Metabolism
0.0
0.5
1.0
1.5
ARCHS4 kinases
EPHA6
TTBK2
NTRK3
BRAF
PRKCA
AKT3
BMPR2
TAOK1
KALRN
SIK3
0
2
4
6
ARCHS4 kinases
NTRK2
TRIB2
NTRK3
KALRN
DCLK2
EPHB1
EPHA6
BMPR2
TNIK
AKT3
0
1
2
3
GO Biological Process
Regulation Of Heart Contraction
Regulation Of Cardiac Muscle Contraction By Regulation Of The Release Of Sequestered
Regulation Of Cardiac Muscle Contraction By Calcium Ion Signaling
Regulation Of Release Of Sequestered Calcium Ion Into Cytosol By Sarcoplasmic Reticulu
Positive Regulation Of Synapse Assembly
Postsynaptic Membrane Assembly
Postsynaptic Density Organization
Positive Regulation Of Blood Circulation
Regulation Of Trans−Synaptic Signaling
Postsynapse Assembly
0.0
0.5
1.0
1.5
GO Biological Process
Regulation Of Potassium Ion Transmembrane Transport
Gamma−Aminobutyric Acid Metabolic Process
Regulation Of Potassium Ion Transport
Regulation Of Monoatomic Cation Transmembrane Transport
Regulation Of Protein Localization To Plasma Membrane
0.0
0.5
1.0
1.5
2.0
GO Cellular Component
Postsynaptic Density
Ionotropic Glutamate Receptor Complex
Postsynaptic Specialization Membrane
Dendrite
Neuron Projection
GABA−ergic Synapse
AMPA Glutamate Receptor Complex
Vesicle
0.0
0.5
1.0
1.5
2.0
-Log10(Padj)
GO Cellular Component
Potassium Channel Complex
Voltage−Gated Potassium Channel Complex
Dihydrolipoyl Dehydrogenase Complex
Astrocyte Projection
Flotillin Complex
External Side Of Apical Plasma Membrane
Mitochondrial Alpha−Ketoglutarate Dehydrogenase Complex
Zonula Adherens
0.0
0.5
1.0
1.5
-Log10(Padj)

Fig. S9

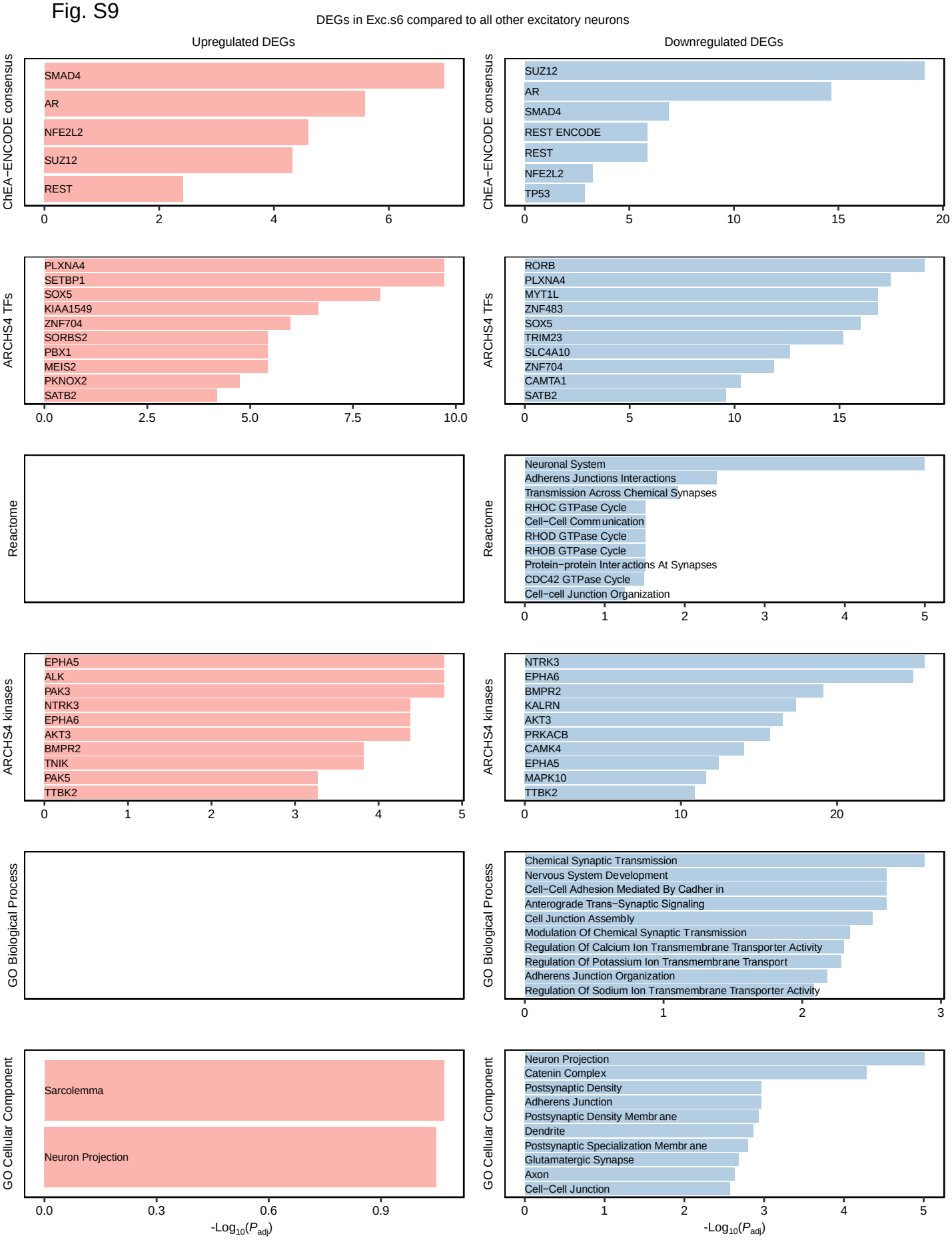
DEGs in Exc.s6 compared to all other excitatory neurons
Upregulated DEGs
Downregulated DEGs
ChEA−ENCODE consensus
SMAD4
AR
NFE2L2
SUZ12
REST
0
2
4
6
ChEA−ENCODE consensus
SUZ12
AR
SMAD4
REST ENCODE
REST
NFE2L2
TP53
0
5
10
15
20
ARCHS4 TFs
PLXNA4
SETBP1
SOX5
KIAA1549
ZNF704
SORBS2
PBX1
MEIS2
PKNOX2
SATB2
0.0
2.5
5.0
7.5
10.0
ARCHS4 TFs
RORB
PLXNA4
MYT1L
ZNF483
SOX5
TRIM23
SLC4A10
ZNF704
CAMTA1
SATB2
0
5
10
15
Reactome
Reactome
Neuronal System
Adherens Junctions Interactions
Transmission Across Chemical Synapses
RHOC GTPase Cycle
Cell−Cell Communication
RHOD GTPase Cycle
RHOB GTPase Cycle
Protein−protein Interactions At Synapses
CDC42 GTPase Cycle
Cell−cell Junction Organization
0
1
2
3
4
5
ARCHS4 kinases
EPHA5
ALK
PAK3
NTRK3
EPHA6
AKT3
BMPR2
TNIK
PAK5
TTBK2
0
1
2
3
4
5
ARCHS4 kinases
NTRK3
EPHA6
BMPR2
KALRN
AKT3
PRKACB
CAMK4
EPHA5
MAPK10
TTBK2
0
10
20
GO Biological Process
GO Biological Process
Chemical Synaptic Transmission
Nervous System Development
Cell−Cell Adhesion Mediated By Cadherin
Anterograde Trans−Synaptic Signaling
Cell Junction Assembly
Modulation Of Chemical Synaptic Transmission
Regulation Of Calcium Ion Transmembrane Transporter Activity
Regulation Of Potassium Ion Transmembrane Transport
Adherens Junction Organization
Regulation Of Sodium Ion Transmembrane Transporter Activity
0
1
2
3
GO Cellular Component
Sarcolemma
Neuron Projection
0.0
0.3
0.6
0.9
-Log10(Padj)
GO Cellular Component
Neuron Projection
Catenin Complex
Postsynaptic Density
Adherens Junction
Postsynaptic Density Membrane
Dendrite
Postsynaptic Specialization Membrane
Glutamatergic Synapse
Axon
Cell−Cell Junction
0
1
2
3
4
5
-Log10(Padj)

Fig. S10

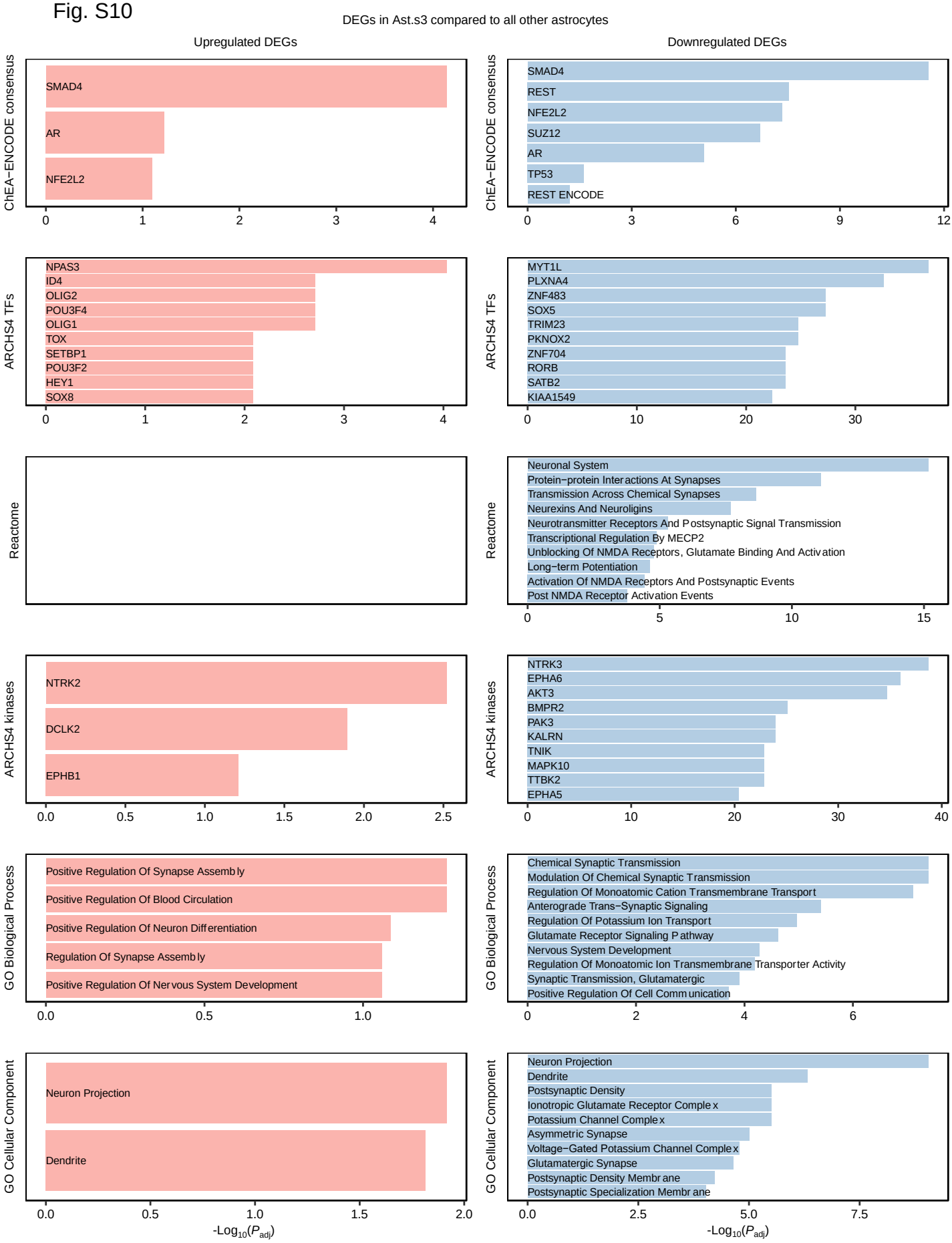
DEGs in Ast.s3 compared to all other astrocytes
Upregulated DEGs
Downregulated DEGs
ChEA−ENCODE consensus
SMAD4
AR
NFE2L2
0
1
2
3
4
SMAD4
REST
NFE2L2
SUZ12
AR
TP53
REST ENCODE
0
3
6
9
12
ARCHS4 TFs
NPAS3
ID4
OLIG2
POU3F4
OLIG1
TOX
SETBP1
POU3F2
HEY1
SOX8
0
1
2
3
4
MYT1L
PLXNA4
ZNF483
SOX5
TRIM23
PKNOX2
ZNF704
RORB
SATB2
KIAA1549
0
10
20
30
Reactome
Neuronal System
Protein−protein Interactions At Synapses
Transmission Across Chemical Synapses
Neurexins And Neuroligins
Neurotransmitter Receptors And Postsynaptic Signal Transmission
Transcriptional Regulation By MECP2
Unblocking Of NMDA Receptors, Glutamate Binding And Activation
Long−term Potentiation
Activation Of NMDA Receptors And Postsynaptic Events
Post NMDA Receptor Activation Events
0
5
10
15
ARCHS4 kinases
NTRK2
DCLK2
EPHB1
0.0
0.5
1.0
1.5
2.0
2.5
NTRK3
EPHA6
AKT3
BMPR2
PAK3
KALRN
TNIK
MAPK10
TTBK2
EPHA5
0
10
20
30
40
GO Biological Process
Positive Regulation Of Synapse Assembly
Positive Regulation Of Blood Circulation
Positive Regulation Of Neuron Differentiation
Regulation Of Synapse Assembly
Positive Regulation Of Nervous System Development
0.0
0.5
1.0
Chemical Synaptic Transmission
Modulation Of Chemical Synaptic Transmission
Regulation Of Monoatomic Cation Transmembrane Transport
Anterograde Trans−Synaptic Signaling
Regulation Of Potassium Ion Transport
Glutamate Receptor Signaling Pathway
Nervous System Development
Regulation Of Monoatomic Ion Transmembrane Transporter Activity
Synaptic Transmission, Glutamatergic
Positive Regulation Of Cell Communication
0
2
4
6
GO Cellular Component
Neuron Projection
Dendrite
0.0
0.5
1.0
1.5
2.0
-Log10(Padj)
Neuron Projection
Dendrite
Postsynaptic Density
Ionotropic Glutamate Receptor Complex
Potassium Channel Complex
Asymmetric Synapse
Voltage−Gated Potassium Channel Complex
Glutamatergic Synapse
Postsynaptic Density Membrane
Postsynaptic Specialization Membrane
0.0
2.5
5.0
7.5
-Log10(Padj)

Fig. S11

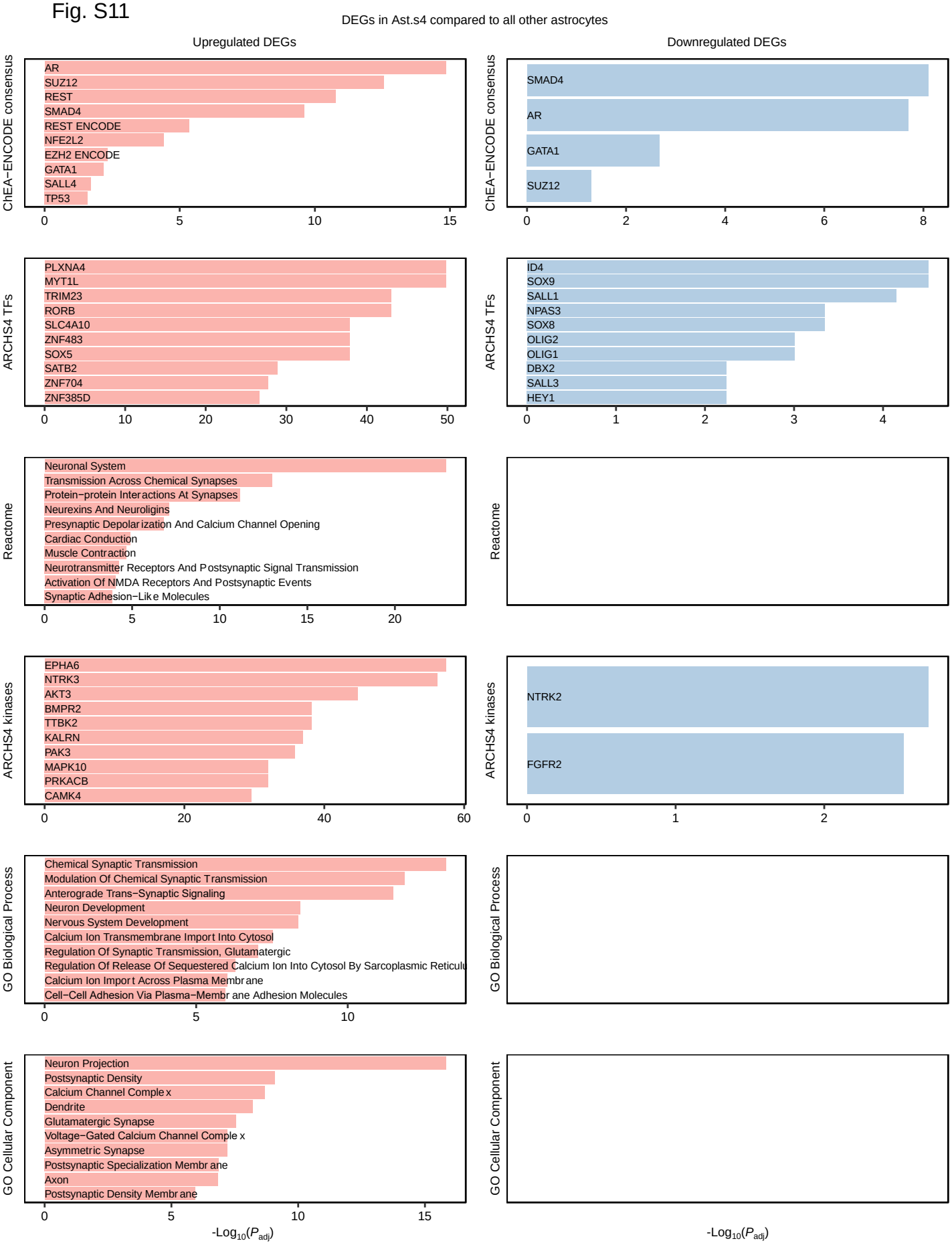
DEGs in Ast.s4 compared to all other astrocytes
Upregulated DEGs
Downregulated DEGs
ChEA−ENCODE consensus
AR
SUZ12
REST
SMAD4
REST ENCODE
NFE2L2
EZH2 ENCODE
GATA1
SALL4
TP53
0
5
10
15
ChEA−ENCODE consensus
SMAD4
AR
GATA1
SUZ12
0
2
4
6
8
ARCHS4 TFs
PLXNA4
MYT1L
TRIM23
RORB
SLC4A10
ZNF483
SOX5
SATB2
ZNF704
ZNF385D
0
10
20
30
40
50
ARCHS4 TFs
ID4
SOX9
SALL1
NPAS3
SOX8
OLIG2
OLIG1
DBX2
SALL3
HEY1
0
1
2
3
4
Reactome
Neuronal System
Transmission Across Chemical Synapses
Protein−protein Interactions At Synapses
Neurexins And Neuroligins
Presynaptic Depolarization And Calcium Channel Opening
Cardiac Conduction
Muscle Contraction
Neurotransmitter Receptors And Postsynaptic Signal Transmission
Activation Of NMDA Receptors And Postsynaptic Events
Synaptic Adhesion−Like Molecules
0
5
10
15
20
Reactome
ARCHS4 kinases
EPHA6
NTRK3
AKT3
BMPR2
TTBK2
KALRN
PAK3
MAPK10
PRKACB
CAMK4
0
20
40
60
ARCHS4 kinases
NTRK2
FGFR2
0
1
2
GO Biological Process
Chemical Synaptic Transmission
Modulation Of Chemical Synaptic Transmission
Anterograde Trans−Synaptic Signaling
Neuron Development
Nervous System Development
Calcium Ion Transmembrane Import Into Cytosol
Regulation Of Synaptic Transmission, Glutamatergic
Regulation Of Release Of Sequestered Calcium Ion Into Cytosol By Sarcoplasmic Reticulu
Calcium Ion Import Across Plasma Membrane
Cell−Cell Adhesion Via Plasma−Membrane Adhesion Molecules
0
5
10
GO Biological Process
GO Cellular Component
Neuron Projection
Postsynaptic Density
Calcium Channel Complex
Dendrite
Glutamatergic Synapse
Voltage−Gated Calcium Channel Complex
Asymmetric Synapse
Postsynaptic Specialization Membrane
Axon
Postsynaptic Density Membrane
0
5
10
15
-Log10(Padj)
GO Cellular Component
-Log10(Padj)